Thesis for the degree of Doctor of Philosophy

Microfluidic devices for single-cell and organ-level studies

Amin A. Banaeiyan

Department of Physics
University of Gothenburg

Gothenburg, Sweden 2017

UNIVERSITY OF GOTHENBURG

Microfluidic devices for single-cell and organ-level studies

Amin A. Banaeiyan

ISBN 978-91-629-0129-5 (printed)
ISBN 978-91-629-0129-1 (PDF)
http://hdl.handle.net/2077/51261

Cover: Formation of bile canaliculi network (green) in 3D tissue-like structures of human induced pluripotent stem cell-derived hepatocytes (blue nuclei) inside a liver-lobule-on-a-chip device.

Department of Physics
University of Gothenburg, SE-412 96 Gothenburg
Tel: +46 (0)31-7860000, Fax: +46 (0)31-7861064
http://www.physics.gu.se

Printed by Aidla Trading AB / Kompendiet
Gothenburg, Sweden 2017

I wish to dedicate this thesis to the memory of my loving mother and to my father for his endless support.

Microfluidic devices for single-cell and organ-level studies

Amin A. Banaeiyan
Department of Physics
University of Gothenburg

Abstract

The process of developing and testing drug candidates is a slow and costly endeavor. The mainstream technologies such as bulk 2D cell culture techniques have been proven insufficient to capture the pharmacokinetics and pharmacodynamics of drug compounds in humans. Animal models, despite their central role in drug development studies, fall short to predict the human-specific mechanisms of drug clearance and toxicity. In this thesis project, I have designed and evaluated application-specific single-cell and organ-on-a-chip microfluidic platforms for drug and chemical compound testing applications. The fundamental advantage offered by single-cell analysis, is the possibility of capturing the behavior of individual cells which, reveals valuable information on the heterogeneity in a cell population. Simultaneously, creating human-based physiologically relevant organ-mimetic microenvironments for drug metabolism and toxicity is becoming increasingly critical. My thesis work, by taking advantage of experimental approaches, qualitatively and quantitatively validates solutions to address the aforementioned challenges in producing relevant data on drug metabolism and toxicity.

A single-cell analysis platform built with the combination of a 4-inlet microfluidic device, a single-beam optical tweezers setup and an epi-fluorescence microscopy stage was used to study the co-administration of the trivalent form of arsenic, As (III), with a Hog1 inhibitor in yeast. In this work we showed that uptake of sodium arsenite could be regulated in single cells. In the next step, I developed a microfluidic device to facilitate high throughput single-cell studies. The device offered the possibility of studying hundreds of cells in each experiment run. Additionally, diffusion-based flow profiles could be administered in this device thanks to the miniature geometry of the microchannels. To promote the formation of 3D tissue-like structures in a physiologically relevant environment, I tailored a microfluidic device to mimic the geometrical hexagonal structure of a classic liver lobule. In this work I showed that human liver cells could be maintained functional in the microfluidic devices for short-term as well as long-term culture periods.

Keywords: Microfluidics, laminar flow, optical tweezers, fluorescence microscopy, single-cell analysis, heterogeneity, *Saccharomyces cerevisiae*, yeast cells, organ-on-a-chip, liver, liver-on-a-chip, HepG2, hiPSC, hiPSC-derived hepatocytes, drug metabolism, drug toxicity

This thesis is based on the work contained in the following scientific papers.

I **Inhibition of MAPK Hog1 results in increased Hsp104 aggregate formation probably through elevated arsenite influx into the cells, an approach with numerous potential applications**
Doryaneh Ahmadpour, **Amin A. Banaeiyan**, Morten Grøtli, Martin Adiels, Mattias Goksör and Caroline B. Adiels
American Journal of Molecular Biology, **4**, 59-71, (2014).

II **Design and fabrication of high-throughput application-specific microfluidic devices for studying single-cell responses to extracellular perturbations**
Amin A. Banaeiyan, Doryaneh Ahmadpour, Caroline B. Adiels and Mattias Goksör
Proceedings of SPIE, International Society for Optics and Photonics, SPIE Microtechnologies, **8765**, (2013).

III **Hydrodynamic cell trapping for high throughput single-cell applications**
Amin A. Banaeiyan, Doryaneh Ahmadpour, Caroline B. Adiels and Mattias Goksör
Micromachines, **4.4**, 414-430, (2013).

IV **Design and fabrication of a scalable liver-lobule-on-a-chip microphysiological platform**
Amin A. Banaeiyan, Jannick Theobald, Jurgita Paukštytė, Stefan Wölfl, Caroline B Adiels and Mattias Goksör
Biofabrication, **9**, 015014, (2017).

My contributions to the appended papers have been as follows.

Paper I : I participated in the experimental design and helped with the experimental plan. I designed the microfluidic device. I performed the numerical simulations. I was actively involved in running the experiments. I helped with editing and proof reading of the paper.

Paper II : I designed, fabricated and numerically and experimentally validated the microfluidic device. I planned and performed the experiments. I wrote the paper.

Paper III : I designed the experiments. I conducted the experimental work. I analyzed the data. I wrote the paper.

Paper IV : I designed and numerically validated the microfluidic device. I fabricated the microfluidic device. I performed the experiments and the data analysis. I wrote the paper.

Contents

Chapter 1

Introduction

The ultimate goal of biology and medicine has chiefly been to improve the quality of human life. Through elemental and experiential expansion of knowledge, the discipline has successfully prevented or remarkably alleviated the inherited and environmental risks on the lives of humans. During the course of history, development of human societies has faced drastic challenges imposed by the outbreak of epidemics, and emergence of unknown diseases. To cope and actively respond to such threats, understanding the working principles of living organisms has been an unceasing commitment for the scientific community. Exploring these mechanisms has been vital to develop effective treatments to eliminate viral or bacterial infections and battle diseases with a challenging genetic nature such as cancer.

The process of drug development however, has been potentially hampered by the drawbacks of currently dominant screening approaches such as two-dimensional (2D) cell culture and animal studies. Traditional cell culture methods, where cells are cultivated on flat surfaces have not experienced considerable changes since their introduction in 1912 by Alexis Carrel [1].

These techniques have proven useful in providing high throughput and reproducible information on early-stage screening studies. However, they offer limited capabilities to control the cellular environment, lack the possibility to create cell-specific physiological niche, fail to systematically study and analyze individual cells or achieve and capture spatiotemporal dynamics [2].

More importantly, the complex absorption, distribution, metabolism, excretion and toxicity (ADMET) mechanisms of drug compounds *in vivo* are unattainable in these systems. Animal studies are an indispensable screening tool in the process of drug development. However, in addition to the ethical concerns associated with animal trials, they have proven to be an insufficient predictive model for conclusive decision making on humans, due to fundamental inter-species genetic variations [3, 4]. Moreover, the many emerging legislations and guidelines regarding animal care and wellbeing in biomedical research, is going to alter the way drug development and toxicity experiments are currently managed. Consequently, overcoming these limitations calls for establishing novel predictive and reliable *in vitro* model systems.

Early-stage studies for new drug development has benefited from the integration of systems biology [5–7] tools and *in silico* studies. Mathematical computation in combination with measured gene expression, proteomics and metabolomics data has been applied

to model the dynamics of biological systems. Currently, due to the complex interactions in biological systems, these approaches are more relevant in cases of simpler organisms and specific signaling pathways. The promising outlook of systems biology research to enhance the process of drug development must be complemented with strong experimental biological knowledge on the cellular as well as tissue level behavior. This will provide relevant information for modeling the cell, physiology of organs and the diseases [8]. The emergence of interdisciplinary approaches such as single-cell analysis and organ-on-a-chip technology can be perceived in this regard.

1.1 Single-cell analysis versus population-level studies

The stochastic nature of gene expression is known to be one of the major sources of cell-cell variations in isogenic populations [9, 10]. The intrinsic noise originates from the inherent stochasticity associated with chemical reactions on the molecular level in a cell. In addition extrinsic noise arising from other sources of fluctuations in cellular dynamics, eg. regulatory factors, gives rise to heterogeneous gene expression levels in a cell population [11]. Such variability in the amount of protein production in different cells by a certain gene is referred to as genetic or transcriptional noise and can lead to subpopulations with dissimilar phenotypes and significant variations in cell development, metabolism, cell cycle, aging and stress responses [12]. Nevertheless, it is clear that an average read out of a cell population is not necessarily the true representative of the cellular behavior of that population but merely a broad picture that can miss important outliers [13]. In diseases like cancer where intra-tumor heterogeneities inflict challenges on effective drug development, understanding the dynamics on the single-cell level aids better characterization of such complexities [14, 15]. To address the need for high throughput, easy and accurate cell sorting in heterogeneous cell populations, methods such as flow cytometry or fluorescent-activated cell sorting (FACS) have been developed [16,17]. Other molecular analysis technologies such as fluorescent *in situ*-hybridization (FISH) [18, 19] and patch clamping [20–22] have also been used on the single-cell level to better understand the cell-cell variability.

Compared to the benefits offered by these prevalent techniques, development of specialized microfluidic devices for single-cell purposes has shown prominent advantages. These devices present the potential to collect single-cell data and monitor real-time cellular behavior with high spatiotemporal resolutions. Introduction of microfluidics and lab-on-a-chip (LOC) or micro total analysis systems (μTAS) [23–27], has created opportunities for unprecedented achievements in chemical and biological sample handling, otherwise impossible by means of mainstream technology.

Under a precisely controllable environment, single-cell microfluidics have facilitated minimized diffusion length scales due to high surface-to-volume ratios [28], minute consumption of rare chemicals and ultimately high throughput data acquisition possibilities [29–32]. In addition, single-cell microfluidics have been successfully combined with other cell manipulation approaches such as optical tweezers, acoustic waves [33], magnetic cell sorting [34], dielectrophoresis [35] and integration of micropumps and microvalves

[36–38]. In collaboration with amplification technologies such as polymerase chain reaction (PCR) [39,40] these platforms have paved the way to acquire large-scale detailed data with strong statistical value. This data has been used to build databases and predictive biological models [41].

1.2 Organ-on-a-chip microfluidic platforms

In light of recent advances and development of customizable microfabricated cell handling devices, the novel category of organ-on-a-chip (OOC) has emerged. The appearance of this class of perfusion devices originates from the pressing need for accurate and human-based predictive screening systems throughout the entire drug development procedure [42]. 2D monolayer cultures do not represent the close physiological conditions of the target organs due to the changes in enzymatic expression and altered cell-cell interactions [43,44]. Moreover, in static cultures dynamics of drug metabolism and clearance are overlooked. For instance, it has been shown that much higher concentrations of drugs are required in 2D cultures to induce comparable efficacy and toxicity responses compared to perfusion models [45].

The initiative towards addressing the lack of predictive human-based *in vitro* tools involves variety of recent advances in developing 3D organoid models [46], spheroid cultures [47, 48], 2D co-culture drug screening plates [49], 3D tissue-like perfusion systems [50–53] and multi-organ-mimicking structures [54]. The effect of the flow condition has been shown previously [45, 55] to enhance cell viability and functionality by constant cell waste removal from the culture environment and fresh media replacement. Moreover, introducing xenobiotics under controlled dynamic flow rates promotes reproduction of *in vivo*-like conditions.

The outstanding prospective of OOC however, is in fact the compatibility of these systems with development of personalized medicine. Incorporating patient-specific human cells in long-term perfusion microfluidic devices and screening for available therapeutics, based on each patient's genetic background, could provide a roadmap to create personalized treatment procedures. As a result, this could also empower approaches to effectively battle cancer, genetic and neurodegenerative diseases.

The main goal of my thesis work has been to develop customized microfluidics and qualitatively as well as quantitatively assess experimental approaches to screen test drugs and chemical compounds in a physiologically relevant dynamic microenvironmet. This work is formulated around addressing these three specific aims:

Aim 1:

The first aim was to assess how the regulation of sodium arsenite, as a major substance in chemotherapeutics as well as an environmental pollutant, could be controlled in a dynamic microenvironment.

Aim 2:

The second aim was to transform the microfluidic chamber to a more versatile design to increase the throughput of the studies, while maintaining the advantages offered by

single-cell analysis.

Aim 3:
The third aim was to adapt and tailor the microfluidic platform to a physiologically relevant environment to facilitate long-term culture and maintenance of adherent mammalian cells as well as promote human-based *in vitro* devices for drug screening applications.

Aim 1 was investigated in **paper I**. We used a custom-made 4-inlet microfluidic device in combination with optical trapping for cell handling. As a whole eukaryotic model organism, *Saccharomyces cerevisiae*, yeast, was used for the studies. We investigated the regulation of As (III) uptake in yeast cells by co-administration of a Hog1 inhibitor compound.

Aim 2 was investigated in **papers II and III**. To address the limitations of cell handling by optical tweezers, a hydrodynamic microfluidic device to capture single yeast and mammalian cells was designed and fabricated. Cell seeding procedure was made significantly easier compared to our previous technique and features such as sheath flow and possibility of diffusion-based mass transport were introduced to the device.

Aim 3 was investigated in **paper IV**. In this paper we mimicked the convection-diffusion mass transport in the structure of a classic liver lobule for long-term maintenance of hepatocytes. The cell culture chambers were arranged in a honeycomb configuration and human cell-lines were used to characterize the device.

Chapter 2

Cell handling

In this chapter principles of fluid mechanics in microfluidics in the scope of this thesis work have been described briefly. Working principles of optical tweezers as a powerful tool to handle biological samples have been explained.

2.1 Microfluidics

The very early microfluidic devices fabricated with the use of modern microtechnology, date back to 1960s to the ink jet printer nozzles developed in IBM and the research on chromatography conducted in Stanford University [56]. Since then the microfluidics field and the innovative use of different materials in fabrication of microfluidic devices have substantially expanded. Early-on fabrication techniques which, primarily employed silicon and glass, have evolved to widespread polymer-and plastic-based devices [57]. Poly-(dimethylsiloxane), PDMS, has been the dominant material for microfluidic experimental prototyping. Unique features of PDMS, including sub-micron feature size yield, gas permeability, optical transparency and the ability of making active fluidic components have made this polymer a desirable choice for researchers in the life sciences [58].

To date, a vast variety of microfluidic systems with different applications have emerged. Highly controlled single-cell analysis systems [29, 59] to investigate genotypic and phenotypic heterogeneities in cells, have made high throughput and parallelized single-cell culture, imaging and data acquisition possible. On chip cell lysis and protein, DNA and RNA isolation using an integrated network of microfluidic valves have been reported.

Droplet-based microfluidics taking advantage of colloidal fluidics have demonstrated promising applications in cell sorting, single-cell analysis, single-cell sequencing and single-cell omics [60].

Digital microfluidics, have emerged as a new approach to manipulate nanoliter-droplets on the surface of arrays of electrodes. A complete cycle of culturing mammalian cells followed by on-chip reagent handling has been demonstrated [61].

Blood plasma separation devices in conjunction with tailored surface chemistry have given rise to point-of-care [62–64] platforms that can be operated without the need for bulky laboratory equipment.

Paper- [62, 64, 65] and plastic [66, 67] microfluidic devices easily fabricated by laser cutting, 3D printing or hot embossing, are on the way to transform healthcare specifically

in low-resource areas such as developing countries and military camps.

Advances in precision fabrication of microfluidic platforms has given rise to a new generation of tools to mimic the physiological environment of cells and eventually reproduce the functionality of specific cell types or whole organs on chip. OOC platforms [50–54, 68–70] are considered amongst the promising technologies for drug testing and the future of personalized medicine.

2.1.1 Fluid dynamics in micron-scale structures

Basic fluid dynamic principles describe the behavior of the flow inside the microfluidic devices. The dominant fluidic regime in micron and sub-micron scales is normally the laminar flow [71]. In contrast to the turbulent and unpredictable streams in macro systems, laminar flow moves in parallel and predictable trajectories and in channels with rigid boundaries forms a parabolic profile as shown in figure 2.1(A).

The dominance of capillary and viscose forces in microfluidics, enables the predictable manipulation of fluids to handle biological samples [72], unlike the macro-scale regime where inertial forces significantly dominate. At small scales several approaches have been followed to analyze the flow behavior based on conservation of mass, momentum and energy. Details of such analysis approaches have been discussed in various fluid mechanics books [73–75]. In the context of this work, the focus has been on the behavior of incompressible, Newtonian and isotropic fluids where the density of the fluid is independent of the pressure and the viscosity is independent of the flow velocity. Governed by the Navier-Stokes equation, the relation between inertial and viscous forces under the velocity (u) and the pressure (p) can be shown as

$$\rho\Big(\frac{\delta u}{\delta t} + u.\nabla u\Big) = -\nabla p + \eta\nabla^2 u + f. \tag{2.1}$$

Based on the characteristics of the fluid, density (ρ) and dynamic viscosity (η), eq. 2.1 determines the velocity of the fluid at a certain time and position. In this equation, f, denotes the body forces such as gravity [75].

Under the certain conditions when we consider the fluid flow to be laminar, the inertial term $\rho\Big(\frac{\delta u}{\delta t} + u.\nabla u\Big)$ in the Navier-Stokes equation can be neglected. Therefore, with the body forces negligible compared to viscous forces, the behavior of the flow is described by the Stokes equation

$$-\nabla p = \eta\nabla^2 u. \tag{2.2}$$

Stokes equation has been the basis of velocity field simulations in **papers I-IV**. For design purposes however, a convenient and practical way to determine the geometrical aspects of the microchannels is to use the dimensionless ratio between the inertial and viscous forces, the Reynolds number, [76] specified by eq. 2.3

$$Re = \frac{\rho u_0 L}{\eta}. \tag{2.3}$$

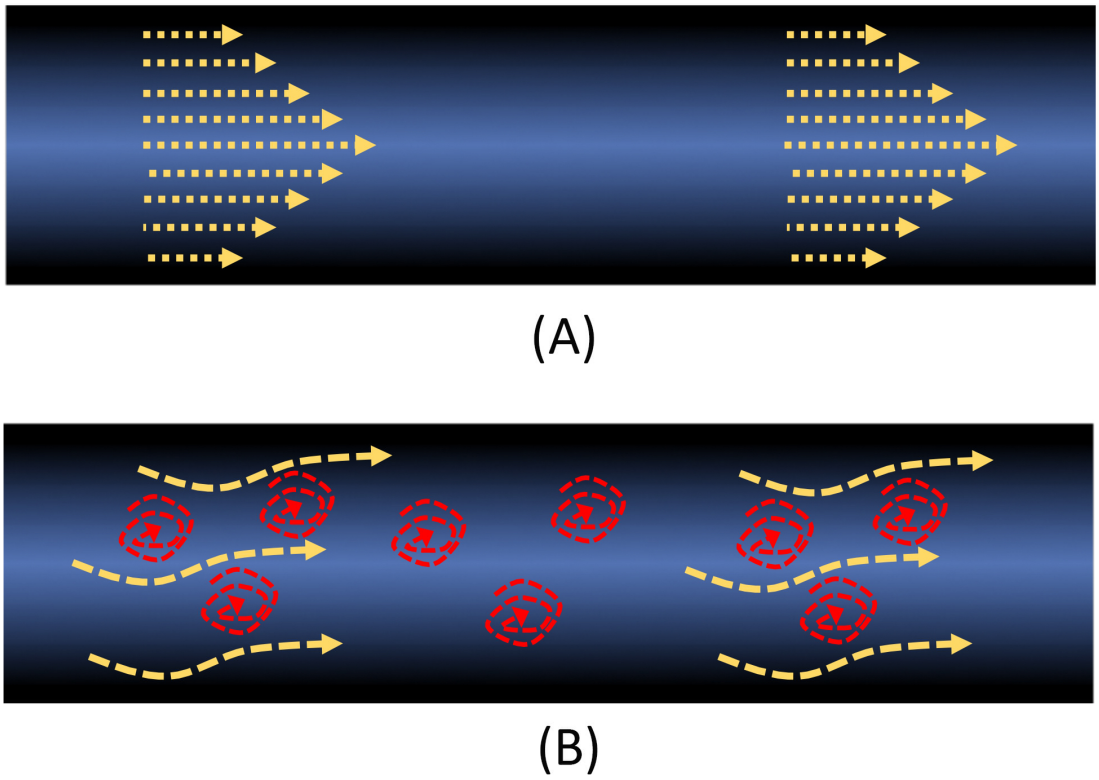

Figure 2.1: Demonstration of the flow in laminar (A) and turbulent (B) regimes. In the laminar flow regime trajectories of the flow form a parabolic shape with the maximum flow velocity in the center of the channels. The turbulent flow profile shows formation of flow eddies and unpredictable behavior along the channels.

In eq. 2.3, u_0 and L are the characteristic velocity and length scale in the microfluidic channel. To calculate the Reynolds number for the microchannels with a rectangular cross section, the length scale L can be approximated by the hydraulic diameter, D_h, [76] of the channels given by eq. 2.4, where a and b are the dimensions of the microchannel.

$$D_h = \frac{4ab}{2(a+b)} \tag{2.4}$$

One can argue that for small Reynolds numbers, typically ($Re \ll 1$), the laminar flow conditions are satisfied, as opposed to the large Reynolds numbers ($Re > 2300$) in the turbulent flow conditions. In the devices presented in **papers I-IV** the Reynolds numbers were below 0.1.

In the laminar flow regime, small spherical particles, are subjected to Stokes drag forces, also known as hydrodynamic forces. For a particle with the radius of r_0 under the relative velocity of U the drag force can be defined as

$$F_D = -6\pi\eta r_0 U. \tag{2.5}$$

In **papers II and III**, hydrodynamic forces (in the oder of pN) have been exploited for trapping and immobilizing cells.

Perhaps the most important property in the micron-scale regime is that mixing of chemical species is dominated by diffusion of the particles rather than convection forces. The diffusion coefficient (D) for different particles has an inverse relation to the radius of the particles and changes in a temperature-dependent manner. This relation can be described by

$$D = \frac{kT}{6\pi\eta r_0}. \tag{2.6}$$

In this equation k is the Boltzmann constant, T is the temperature and r_0 is the radius of the particles. Based on the Fick's law of diffusion, the flux of particles, **J**, from a higher to a lower concentration of c with a diffusion coefficient of D, is explained as

$$J = -D\nabla c. \tag{2.7}$$

In the micron-scale geometry of the microfluidic channels, under the assumption of time-independent D, with combination of the convective term (cu) and the Fick's diffusion law in the continuity equation, the convection-diffusion equation can be simplified to

$$\frac{\partial c}{\partial t} = D\nabla^2 c - u \cdot \nabla c. \tag{2.8}$$

This principle has been considered in the numerical simulations for the diffusion of substance in relation with the velocity field inside the microfluidic devices in **papers I-IV**.

For the design purposes of the microchannels in regard to convection and diffusion, following a similar approach to the Reynolds number, the Péclet number has been used.

The Péclet number is a dimensionless value, which denotes the ratio between the convective and diffusive mass transport in a fluidic system. This relation is described in eq. 2.9

$$Pe = \frac{uD_h}{D}. \tag{2.9}$$

For low Péclet numbers ($Pe \ll 1$), the time required for transport of particles by diffusion is shorter than the time required for advection, whereas in larger Péclet numbers ($Pe \gg 1$), transport of particles is advection dominated. The measure in contrary to the Reynolds number does not have a typical indicative range for microfluidic devices and can vary based on the required channel geometries and designated applications.

2.2 Optical tweezers

The simple working principles of optical trapping has offered promising advantages in the nanometer to hundreds of microns length scales [77]. Multi-particle trapping, complex 3D holographic field generation, measurement of small interaction forces and active cell sorting are perhaps the areas that optical trapping has received the most profound enthusiasm and

development in the recent years [78]. Optical tweezers in handling biological objects [79,80] has been used widely as a non-invasive manipulation technique.

This includes applications such as systematic cell positioning inside microchambers [81–83], mechanical cell deformation and membrane elasticity measurements [84–86], membrane tether extraction [87], cell fusion experiments [88], *in vivo* manipulation of red blood cells [89], biochemical and mechanical induction of signaling events in mammalian cells [90, 91], measurement of live cell-mediated mechanical forces [92], to name a few.

2.2.1 Working principles of optical tweezers

The basic principle behind optical tweezers is that light carries momentum in addition to energy and through transfer of this momentum, forces can be applied to objects. This phenomenon was demonstrated experimentally by Ashkin *et al* for dielectric particles in 1986 [93]. Based on the dimensions of the interacting object different theories are used to explain the momentum transfer and optical forces. For instance in case of small spherical particles with a radius of r_0 where $r_0 \ll \lambda$ (λ is the wavelength of the incident light), Rayleigh scattering is used and when $r_0 \gg \lambda$ ray optics regime applies in the approximations [94].

In cases where the dimensions of the particle are in the order of the light wavelength, the theories used to explain the two former conditions have proven insufficient to calculate the optical forces. Therefore, a generalized Lorentz-Mie scattering in a Gaussian beam [95] or applying a dipole approximation on any sizes of dielectric particles in a focused laser light have been proposed [96]. Figure 2.2 shows an example where the size of the particle r_0 is larger than λ. The particle is attracted to the center of the focus of the beam and settles below the beam waist. The effect of reflection of the laser on the surface of the particle has been neglected in this figure.

To trap micron-scale particles e.g. living cells, a strongly focused laser beam, typically through a microscope objective with high numerical aperture (NA) provides the sufficient light intensity. The direction of the forces exerted on the particle is always in the opposite direction of the particle displacement. Therefore, the gradient forces are referred to as restoring forces that maintain the particle close to the center of the focus under the equilibrium conditions.

The exerted force on the cells is calculated through the Hooke's law

$$F = -k\Delta x. \tag{2.10}$$

As seen in eq. 2.10, the optical forces typically in the order of fN to hundreds of pN are negatively proportional to the displacement of the particle (Δx) with a constant k referred to as the trap stiffness.

A particularly important detail to account for when using optical tweezers in live-cell handling is to minimize the risks of photo-damaging and heat generation due to absorption. Therefore the infrared and far-infrared wavelengths are chosen due to relatively low absorption in the cells. Additionally, low optical powers (in mW range) typically required for optical trapping systems serve this purpose adequately. In our experiments in **paper I**, we used optical tweezers to create customizable arrays of cells placed in controlled distances in respect to each other. This, primarily was to assure that cell-cell interactions did

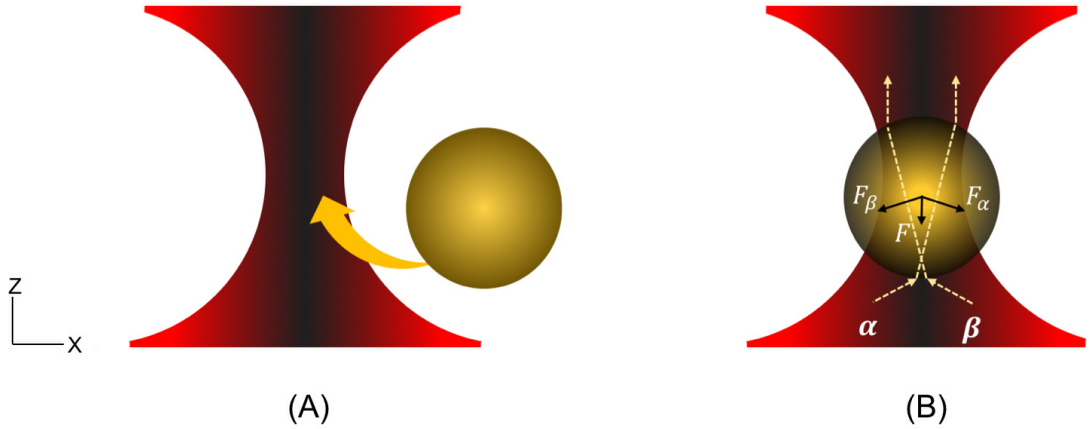

Figure 2.2: For particles in the close proximity of a highly focused laser beam a gradient force towards the center of the focus attracts the particles to the trap (A). The amount of forces exerted on the trapped particle are equal and opposite to the direction of the radiation pressure from the momentum transfer to the particle. The total force applied to the particle is F and is the combination of F_α and F_β (B). F_α and F_β are the gradient forces of the incident rays α and β respectively.

not influence the single-cell behavior to the environmental changes and that the individual cell responses were recorded. Combination of optical tweezers with a 4-inlet microfluidic chamber and fluorescence microscopy was used in **paper I** to conduct real-time single-cell experiments.

Chapter 3

Cell imaging

3.1 Brightfield and fluorescence microscopy

Fluorescence microscopy is amongst the most popular and widespread tools used in modern biological studies. The combination of light microscopy with fluorophores [97] has revolutionized the fundamental approaches made towards resolving the details of sub-millimeter and sub-micron organisms. In a light microscope setup including an objective and an ocular a magnified image of the samples can be produced and captured by means of photosensitive detectors or optical cameras [98]. Despite the emergence of label-free detection techniques such as mass spectroscopy (MS) [99], quartz crystal microbalance (QCM) [100] or surface plasmon resonance (SPR) [101], fluorescence microscopy techniques have persisted as a key approach to visualize and acquire data on the dynamics of cellular and molecular systems [102]. The possibility of fusing proteins of interest with fluorescent proteins e.g. green fluorescent protein (GFP) [103] has provided the scientists with an exceptional tool to trace and record the protein up-regulation, misfolding, degradation and interactions in living cells in real time.

GFP and its counterparts have a fairly simple working principle which relies on excitation and relaxation of photons at different wavelengths. Based on the Jablonski diagram [104] depicted in figure 3.1, the fluorophore molecule or any particular fluorescent protein has to be brought up to the excitation state by the incident photons of energy $h\nu_1$ where ν is the photon frequency. After excitation of the ground state electrons to a higher energy level, a photon of lower energy $h\nu_2$ ($\nu_2<\nu_1$) is emitted upon relaxation of the excited electrons. The emission photons can then be detected apart from the incident photons due to the wavelength differences [102].

In a regular setup of an epi-fluorescent microscope as seen in figure 3.2, a broad-band excitation light source is used to illuminate the sample. To increase the angle of light collection and therefore the amount of collected light in the objective, a high NA objective is used. Equation 3.1 shows the relation between the NA, refractive index of the surrounding medium (n) and (θ), the half angle of the cone of light collected by the objective.

$$NA = nsin\theta \tag{3.1}$$

An immersion medium such as water or oil with a higher refractive index compared to

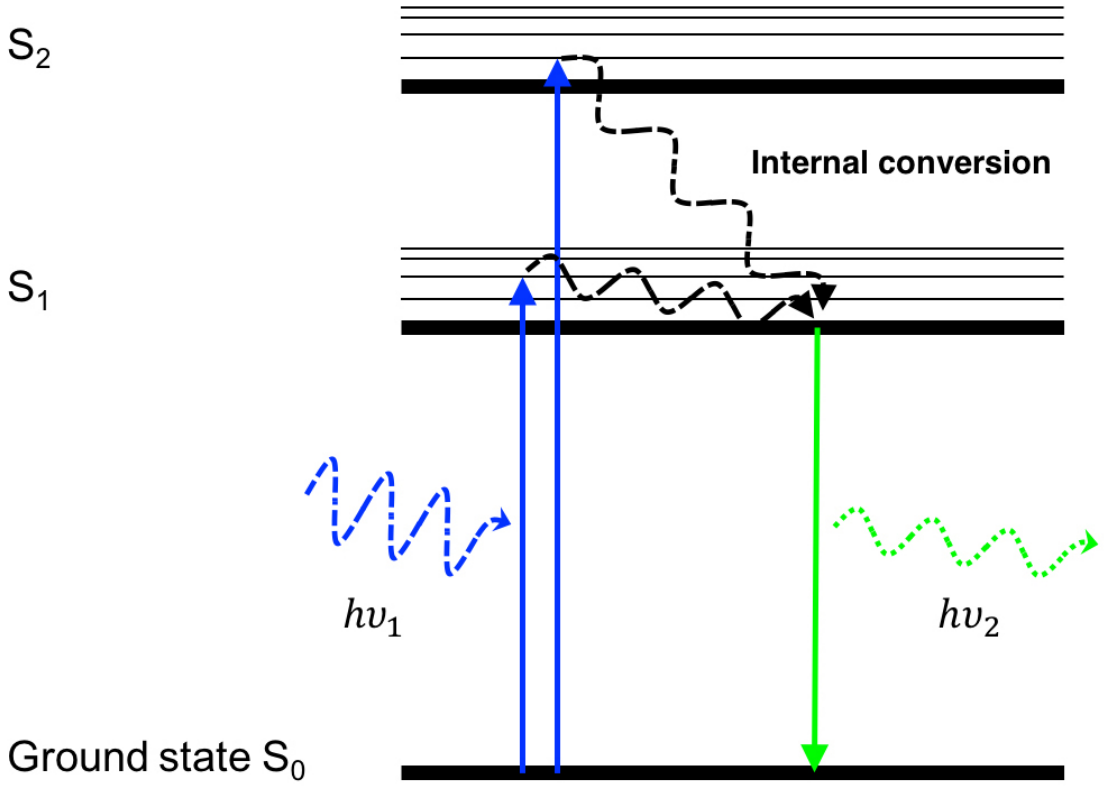

Figure 3.1: Illustration of fluorescence in a Jablonski diagram. The electrons of the ground state (S_0) in the fluorophore become excited upon receiving energy from the excitation light with the energy of $h\nu_1$. After relaxation from the excited states (S_1 and S_2) to the ground state via internal conversion, the electrons emit a photon of lower energy $h\nu_2$ and longer wavelength.

the specimen is used together with the high NA objective to allow for the maximum light collection angle. In the epi-fluorescent microscope, the emission light from the sample is collected through the same illumination objective. The incident light is filtered out through the emission filters and only the red-shifted wavelength from the fluorescent molecules is detected [97].

3.1.1 Confocal fluorescence microscopy

Unlike the epi-fluorescence microscopy where the entire field of view is illuminated by a broad band lamp, in confocal microscopy a laser beam with a specific wavelength is focused by a high NA objective to excite the sample. Since the laser beam is focused on a single spot on the specimen, the sample needs to be scanned in order to create an image. Therefore instead of an optical camera a photodetector or otherwise called a photomultiplier tube is used for signal detection. The emission signal from each illuminated point is collected and stored in a computer. This data is then used to reconstruct the image.

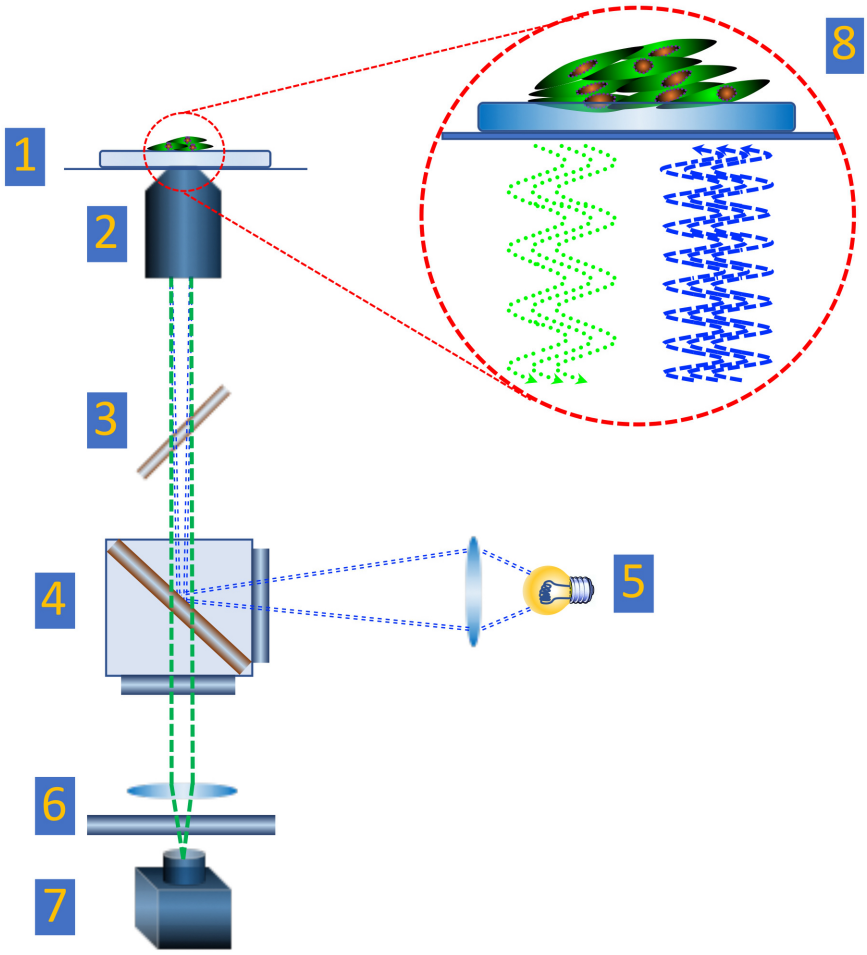

Figure 3.2: In an epi-fluorescent microscope setup the sample (1) is illuminated through the objective (2). Components such as dichroic mirror (3) and the filter cube (4) which, contains the excitation and emission filters for the designated illumination wavelengths are located In the optical path. The halogen lamp (5) is usually a broad-band light source, used to excite the sample. Through the filter cube, the fluorescent signal from the samples passes the tube lens and the blocking filter (6) and is detected by means of a detection device e.g. an EMCCD camera (7). (8) shows a close-up view of the excitation and emission in the sample plane.

For collection of the emission signal from the sample, confocal imaging takes advantage of a fairly simple principle. When the multiple points along the depth of the sample are

excited, the emission signal from the points that are out of focus are blocked by a pinhole placed at a conjugate plane to the sample plane. This way, only a small fraction of the emission light from the out-of-focus points reaches the detector and a high contrast is achieved in the final image. To image the whole depth of the sample the objective is refocused on multiple sections with defined splitting distances. By constructing the image out of each scanned optical section, a 3D image can be reconstructed. More details on biological confocal microscopy can be found at [105].

In the scope of this work brightfield, epi-fluorescence and confocal microscopy have been used to visualize protein aggregates (**papers I and III**) and for live cell staining image acquisition.

Chapter 4

Biological model systems

This chapter describes the biological systems that have been studied in this thesis. *Saccharomyces cerevisiae* or yeast cells have been chosen for the experiments in **papers I-III**. The availability, ease of cultures and preparation, flexibility and access to a large variety of strains are the advantages offered by yeast. In our experimental settings, yeast cells were exposed to extracellular stimuli in two different microfluidic chambers and cellular responses were recorded by time-lapse imaging.

To promote physiologically relevant human-based *in vitro* models to study efficacy and cytotoxicity of drug candidates, we used human liver cells. Human hepato-cellular carcinoma cell-line (HepG2) and human induced pluripotent stem cell (hiPSC)-derived hepatocytes were cultured in the microfluidic devices.

4.1 *Saccharomyces cerevisiae*

Saccharomyces cerevisiae also known as brewers or bakers yeast has a historical role in various developmental phases of the ancient and modern human society. Yeast has long been used to make bread, beer and wine, yet one of the most important contributions of this eukaryotic organism has been in the advancement of knowledge in the life sciences [106]. Yeast cells have unique properties similar to higher eukaryotic organisms including cell components such as nucleus and mitochondria as well as the cell cycle, DNA replication and interacellular signaling.

A disruptive development has occurred in eukaryotic biology after the sequenced genome of yeast was published for the first time in 1996 [107]. This breakthrough provided the opportunity to genetically modify and study the biology of different strains, explore the underlying mechanisms of signaling pathways, discover relations between the gene expression and protein functions in the cell and introduction of completely new fields of research such as "systems biology" and "functional genomics" [108, 109].

Additionally, the comparison between the yeast and human genome revealed that most of the gene and protein functions were conserved in yeast. Homologues of many of the genes involved in the diseases in humans have been found in yeast. It has also been shown that a recognizable percentage (47%) of genes in yeast have human orthologs and can be replaced by the human genes [110]. Therefore, yeast has presented itself as an easy-to-use experimental system where a majority of molecular mechanisms involved in human

diseases such as cancer and aging could be studied.

A single yeast cell represents a complete eukaryotic organism which, makes it a desirable model for studies targeting certain diseases such as Alzheimer's [111, 112], Huntington's [113–115] and Parkinson's as well as investigating the factors involved in apoptosis and the process of aging [116–118]. Figure 4.1 shows a microscope image of budding yeast cells. Yeast cells are typically grown in media rich in glucose and amino acids. Yeast nitrogen base (YNB) is typically the choice when culturing yeast for fluorescent microscopy purposes due to the low auto-fluorescence of this medium. YNB is supplemented with glucose and amino acids. Yeast cells divide in a process referred to as budding. Each cell produces fresh buds or daughter cells that eventually grow to adult cells and undergo the growth cycle. In the logarithmic growth phase, yeast cells divide at their maximum rate until due to the consumption of the nutrients in the growth media, cells enter the stationary phase and the growth rate plateaus.

Many of the signaling pathways are conserved in yeast, and this is one of the most interesting properties that can be used for studying the mechanisms of cellular behavior in humans. Signaling pathways are often described as a cascade of protein interactions and explain how cellular responses are mediated. For instance, in the high osmolarity glycerol (HOG) pathway [119] in yeast, the two membrane receptors referred to as Sln1 and Sho1 are activated in response of the cell to the external stress and osmotic changes. The HOG pathway belongs to a large family of signaling pathways called mitogen activated protein (MAP) kinase. In the HOG MAPK pathway, when the osmolarity of the environment increases, a series of kinases activate their downstream components. Specifically, MAPK Hog1 protein is activated through phosphorylation and migrates to the cell nucleus [120]. Hog1 accumulation in the nucleus results in specific gene expression which increase the glycerol level in the cell [121] and adapts the intracellular osmolarity to the new osmotic conditions.

In my thesis I have used a small molecule MAPK Hog1 inhibitor compound [122] that impairs the activity of this protein and potentially results in the increase of external sodium arsenite uptake by yeast cells (**paper I**).

4.2 Human liver

4.2.1 Physiology of the liver

The liver is the largest inner organ of the body. The liver has the important role of metabolism and detoxification of the compounds entering the vasculature system of the body, including nutrients and xenobiotics. The liver consists of parenchymal (PC) and non-parenchymal cells (NPC). Hepatocytes, the PC part of liver, comprise around 60% of the cells in the organ. Hepatocytes have a polygonal appearance and show at least one or two prominently round nuclei. These cells are key to the exocrine and endocrine functions of the liver. Hepatocytes exhibit cell polarity and form distinct luminal domains restricted by the tight junctions between the adjacent cells. This polarized organization, results in formation of narrow channels of bile canaliculi. Hepatocytes exert bile into the canaliculi network which, through the bile ducts flows to the gallbladder, the common bile duct and the intestine [123]. Expression of the liver-specific protein albumin and phase I and

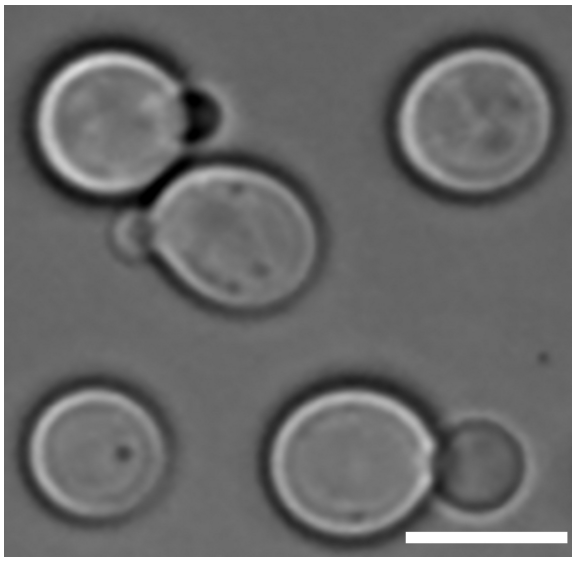

Figure 4.1: Brightfield microscope image of budding yeast cells. Magnification of the objective = 100 ×. Scale = 5 μm.

phase II metabolism of drugs are other important functions of the liver hepatocytes [124]. The non-parenchymal part of liver includes multiple cell types such as liver sinusoidal endothelial cells (LSEC), Kuffer cells (KC) and stellate cells (SC). Each of these cell types has specialized duties [125]. Hexagonal classic liver lobules incorporate the liver vasculature system. The portal triads including the hepatic artery, hepatic portal vein and the bile ducts extend through the hepatic cords and via the sinusoid structures maintain the continuos exchange of oxygenated blood, hormones, vitamins and liver enzymes within the tissue [126]. The hepatic cords extend in a radial fashion towards the center of each lobule where a branch of central vein is located. The processed molecules including cell waste and drug metabolites drain out through the central vein to the hepatic vein and join the blood circulation in the inferior vena cava [126]. Endothelial cells comprise the majority of the NPCs in the liver. The lining layer of cells around the liver sinusoidal cords and extending from the portal triads are the LSECs. These cells exhibit a unique fenestrated membrane structure and are responsible to shield the hepatocytes from the shear-imposed stress of the blood flow while allowing the diffusion of vitamins, hormones, drugs and nutrients from the blood capillaries [127, 126]. Apart from having the role of barriers between the blood flow and the PC, these cells have unique scavenger properties which involves them in the uptake of antigens, elimination of endotoxins, activating leukocytes by secreting cytokines and chemokines and regulating the inflammatory response of the liver [128]. The KCs are the tissue macrophage cells present in the liver. KCs have been studied for their central role in the hepatic responses to toxicity and acute or chronic liver tissue damages. These cells are known to be responsible for secretion of cytokines such as tumor necrosis factor α (TNFα) and release of reactive oxygen species (ROS) in response to liver damage and contributing to activation of apoptosis in hepatocytes. On the contrary, there are recent reports that KCs are not only respondents and mediators of

the liver toxicity and injury but, they can also assume a protective function in the anti-inflammatory responses of the liver [129]. SCs reside in the space between the PCs and the LSECs known as the space of Dissé. SCs are known to have the major contribution in collagen production and creating extra-cellular matrix (ECM) in case of chronic liver injury which, promotes the liver regeneration and alleviates the damage. These cells are also the major source of vitamin A storage in the body. There is also evidence that SCs are actively involved in the chronic liver inflammatory response by secreting inflammatory cytokines to modulate the liver injury. Secretion of transforming growth factor β (TGF-β) and connective tissue growth factor (CTGF) upon activation and increased levels of ECM expression by SCs in chronic damage can lead to liver fibrosis [130].

4.2.2 Primary human hepatocytes and alternative liver cell-line models

Early-stage drug efficacy and toxicity predictions is a pressing demands due to the significant impact of drug-induced liver injury (DILI) on the process of developing new drug candidates. The high failure rates in animal studies, clinical trial phases or even after the drug approval are some of the challenges standing in the way of getting treatments to the patients in need [131].

Primary human hepatocytes (PHH) are the gold standard, a well established biological model system, to study metabolism of endogenous and exogenous compounds, detoxification and clearance of drugs, mechanisms of protein synthesis and enzyme regulations [132]. Freshly isolated or cryopreserved primary hepatocytes are widely used as *in vitro* sources for drug metabolism, co-administration and drug-drug interactions [133]. The serious limitations with PHH are, however, the shortage of high-quality cell lots and a significant lot-to-lot variation that impede the consistency and accuracy of high throughput substance screening. Additionally PHH tend to maintain short-term functionality *in vitro* hence, failing to meet the requirements for long-term culture periods [134].

To overcome such problems immortalized cell lines from liver carcinoma have been used. Human hepatocellular carcinoma cell-line (HepG2) is a widely used liver cell-line for *in vitro* studies. Ease of culture and possession of hepatocyte-like functionality features such as secreting liver-specific proteins has made HepG2 an alternative human-based cell line for toxicity studies and compound screening. However, HepG2 are known to have a low metabolic activity compared to PHH [135] and can poorly predict DILI, although they show responses to drug treatment and express cytochrome 450 (CYP 450) [136].

Another more recent model cell-line derived from human liver hepatoma is the HepaRG. HepaRG cells compared to HepG2 express higher liver-specific functions including major phase I and phase II liver enzymes [137]. HepaRG therefore, are considered a closer model to PHH and have found extensive use in metabolic and toxicology studies. The cells have the ability to proliferate and differentiate when they are seeded in lower densities (2.6×10^4 cells cm^{-2}) [137] and generate two distinct sub-populations. More than 50% of the sub-populations are hepatocyte-like cells with one or two nuclei and express liver biomarkers. The other sub-population has the phenotypic resemblance to endothelial cells with an elongated distinct cytoplasm. HepaRG have also been shown to demonstrate higher sensitivity in DILI prediction studies compared to HepG2 [136].

Since the discovery of iPSC technology by reprogramming adult fibroblasts to a stem-cell like state, first presented by Takahashi and Yamanaka [138], growing interest has led to further development of several differentiation protocols for multiple cell types. This approach has offered numerous advantages over the conventional *in vitro* models. For example hiPSC-derived hepatocyte-like cells have been shown to express major functions of the PHH, higher levels of enzyme production compared to cell-lines, and higher life span compared to PHH [139]. hiPSC-derived hepatocytes provide an unlimited source of high quality cells while eliminating the lot-to-lot variations associated with PHH. Additionally, developing mature hepatocyte-like cells from different donors extends the possibility for high-throughput and high-content screening studies. Figure 4.2 shows the brightfield microscope image of PHH (A), HepG2 (B) and hiPSC-hepatocytes (C) cultured in 2D flasks under designated growth protocols.

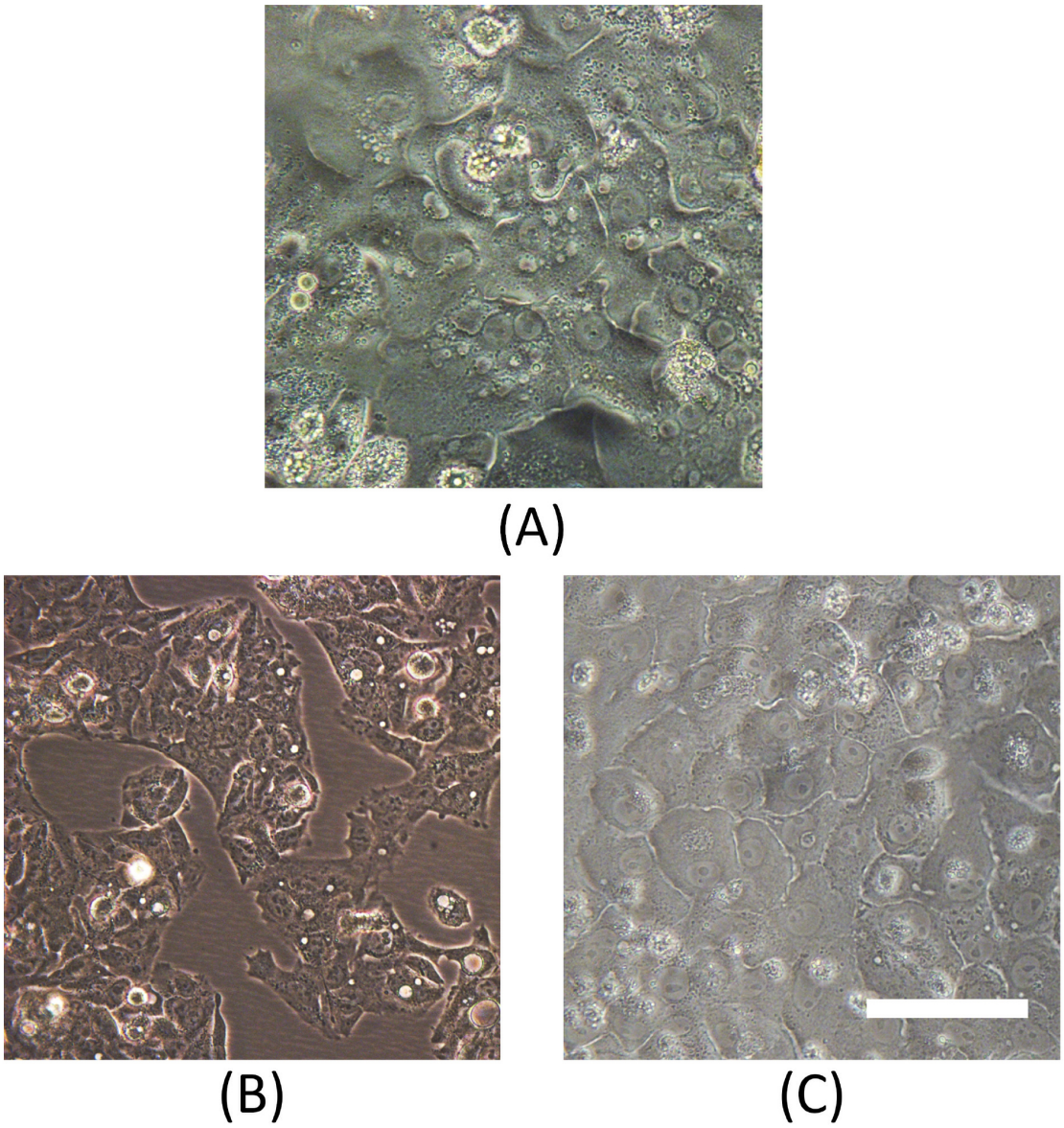

Figure 4.2: Brightfield microscope image of liver cell lines. The monolayer culture of primary human hepatocytes (Cells provided by Bioreclamation-IVT) (A), HepG2 (Sigma Aldrich, Germany) (B) and human induced pluripotent stem cell (hiPSC)-derived hepatocytes (Cellular Dynamics International, USA) (C). Scale = 50 μm.

Chapter 5

Methodology and experimental procedure

This chapter explains the flow simulations, operation principles of the microfluidic devices, optical tweezers set up, required materials and the equipment to design and conduct the experimental work reported in **papers I-IV**. Cell culture and maintenance protocols have been described according to the experimental conditions. To operate the microfluidic devices, a number of steps were followed including sterilization of the microfluidic devices, preparation of the cells, setting up the fluid delivery tubing, pumps, imaging equipment and the automation software.

Flow rates were programmed accordingly for each experiment and time-lapse imaging was controlled by OpenLab software (PerkinElmer, Waltham, MA, USA). Assays, including enzyme-linked immunosorbent assay (ELISA) and urea detection assay were conducted according to the manufacturers' protocols.

5.1 Finite element COMSOL simulations in microfluidic devices

5.1.1 4-inlet microfluidic chamber

For rapid environmental perturbations we used a 4-inlet microfluidic system. In the numerical simulations the height of the device was set to 27 μm. As seen in figure 5.1 the cell array with the desired number of cells was placed in the second junction of the 4-inlet system. The coordinates for the array position were fed to the automation software. To predict the behavior of the laminar flow in the chamber, flow velocity and diffusion of substances were simulated jointly in the finite element software COMSOL multiphysics (COMSOL Inc., Burlington, MA, USA). The position of the cell array and the exposure area in the devices were decided based on the simulations. This step was imperative for accurate and uniform cell exposure to the intended concentrations and to minimize the diffusion-based mixing in the cell area. For all simulation conditions, incompressible, Newtonian and laminar flow regime was selected. For all the channel walls a no-slip boundary condition was chosen. The mesh elements in the simulations were selected as the default tetrahedral settings. The inlets of the devices were set to the desired flow rates. The

outlet pressure was set to 0 Pa. Constant fluid density and mass conservation under Navier-Stokes equation (eq. 2.1) was applied. The "laminar flow" module was selected for the flow velocity simulations. The "laminar flow" module takes into account all the boundary conditions for the no-slip flow channels and calculates the flow velocity under the stationary conditions ($\delta u/\delta t=0$) applied in eq. 2.1.

"Transport of diluted species" physics for diffusion studies, takes into account the velocity field simulation output of the COMSOL study in the channels and calculates the diffusion of chemicals with the assumption of the constant diffusion coefficient D. The standard convection-diffusion equation (eq. 2.8) was used for the studies. Concentrations of the chemicals were selected for the experimental conditions. Diffusion coefficients were found from the literature.

As seen in figure 5.1 for Hog1 inhibitor (10 μM concentration) and sodium arsenite (0.1 μM concentration) in the 4-inlet system, flow rates in the channels 1 to 4 were set to 5, 5, 500, 5 nl min^{-1} for the inhibitor and 5, 5, 5, 1000 nl min^{-1} for sodium arsenite. Diffusion coefficients were $D = 2.4 \times 10^{-10}$ and $D = 1.21 \times 10^{-9}$ m^2 s^{-1} for the inhibitor and sodium arsenite respectively. The cell array was fully covered by the substances under these parameters verified by control experiments with fluorescein solution (not shown).

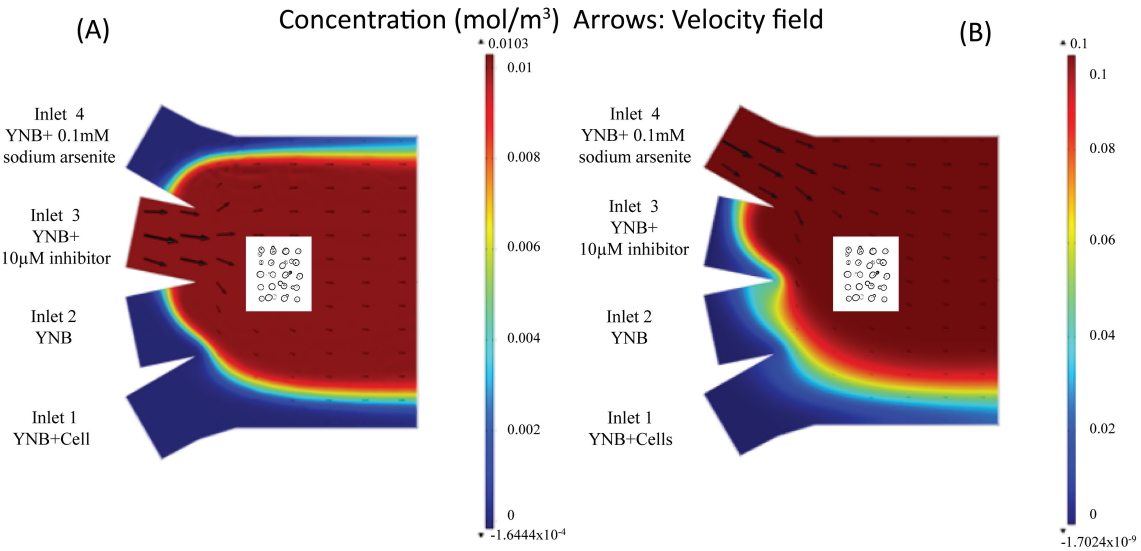

Figure 5.1: Diffusion of sodium arsenite and the Hog1 inhibitor in the microchannels were simulated under the flow rates of 5, 5, 500, 5 nl min^{-1} for the inhibitor (A) and 5, 5, 5, 1000 nl min^{-1} (B) for sodium arsenite in inlets 1 to 4 respectively. The coordinates for positioning the cell array were found from the numerical simulations primarily to ensure the full coverage of the cells with the test compounds.

5.1.2 CellComb device for hydrodynamic cell trapping

To trap and immobilize yeast cells in a high throughput microfluidic device, a multi-trap microfluidic system was designed and fabricated. Three parallel microfluidic channels were

connected via V-shaped pockets as described in **papers II and III**.

The flow velocity at the nuzzle junctions between the 2-μm openings and the side channels reaches its maximum as depicted in figure 5.2. The height of the device has been set to 5 μm in the simulations.

COMSOL boundary conditions mentioned in section 5.1.1 were applied. Figure 5.2 shows the velocity field for an example flow rate of 25 nl min^{-1}. The flow trajectories were added to the simulations by the streamline function to depict the flow stream. The simulations have been carried out without introducing the cells to the studies. The assumption was that cells of comparable diameter with the height profile of the device will significantly block the traps and the high-flow region will move along the device. This assumption was tested for by introducing spherical obstacles to the geometry of the device. As seen in figure 5.2 the jet flow area is transferred successively to the empty traps downstream the device. Same sets of simulation studies were conducted for the device geometry tailored for mammalian cell entrapment. The height profile of the device was changed to 15 μm, while the other parameters were kept unchanged.

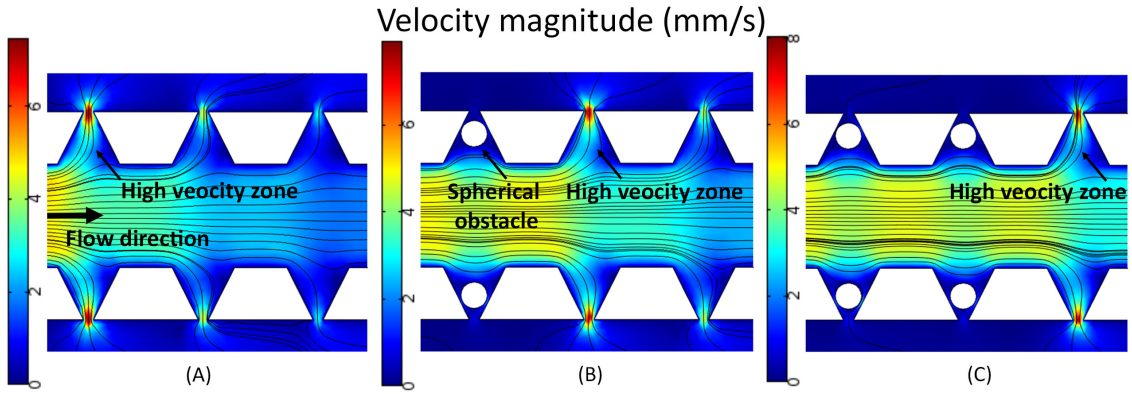

Figure 5.2: In the CellComb device, hydrodynamic cell entrapment was the principle of operation. Cells were immobilized by the drag forces of the flow and kept inside the microtraps for the successive substance exposure steps. In the flow simulations in (A), (B) and (C) under the flow rate of 25 nl min^{-1}, spherical objects were positioned at the nib of the microtraps and the transition of the high-flow region alongside the device was followed. This principle facilitated the cell loading step in the microfluidic devices.

5.1.3 Very large scale liver-lobule (VLSLL)-on-a-chip device for 3D liver tissue formation

VLSLL-on-a-chip device aimed at creating a biomimetic structure to reproduce the convective-diffusive blood circulation in the liver structure. The design of the device

was inspired from the hexagonal classic liver lobule structures. Cell culture chambers were in contact with the surrounding feed network through arrays of diffusion passages with the cross section of 2 μm $\times$ 2 μm. The incorporated diffusion passages alongside the lobule-like chambers mimic the fenestrated LSECs, allowing for the diffusion-based mass transport into the cell culture chambers and protect the hepatocytes from shear force of the flow, which has previously been shown to have a negative effect on cell viability and functionality [140].

In the simulation studies, the central vein mimetic in the center of each chamber has been assigned to drain the fluids out of the culture chambers. As shown in figure 5.3 the amount of shear rate and flow velocity drop significantly while moving alongside the diffusion passages (from feed network towards the cell culture chambers) and is minimized inside the cell culture chambers.
Based on the simulation results of the shear rate, γ (s^{-1}), the shear stress for the different regions of the device was calculated using

$$\tau = \gamma\eta. \tag{5.1}$$

A significant decrease in the shear stress from $\tau = 0.04$ dyne cm^{-1} in the surrounding feed network to ≈ 0 in the culture chambers was obtained in the simulations.

Simulation results showed that the role of convective flow inside the culture chambers was insignificant and therefore the mass transport was dominated by diffusion e.g. as seen in figure 5.3 for glucose with $D = 9 \times 10^{-10}$ m^2 s^{-1}. These results were in agreement with the calculated Péclet number from eq. 2.9 as a measure of convection and diffusion in the microchannels. From the calculations, $Pe = 30$ in the feed network dropped to $Pe = 1.8 \times 10^{-3}$ inside the culture chambers denoting the diffusive transport in the cell culture area.

5.2 Experimental procedures for microfluidic device fabrication, operation and cell handling

5.2.1 Fabrication of microfluidic devices

Photolithography and soft polymer molding is one of the main fabrication techniques in microfluidic devices, originally developed in semiconductor industry and silicon electronics [76]. The feasibility of photolithography techniques in combination with biocompatible materials such as PDMS has made them a widespread and robust method of microfluidic fabrication. Compared to bulk and surface micromachining approaches which involves wet or dry etching steps, lithography techniques provide an easier and faster fabrication process without the need for expensive cleanroom facilities and in-house micromachining tools. Photolithography involves a chromium or transparency mask set with the desired patterns. The mask type is usually decided depending on the required resolution and feature size. Transparency masks

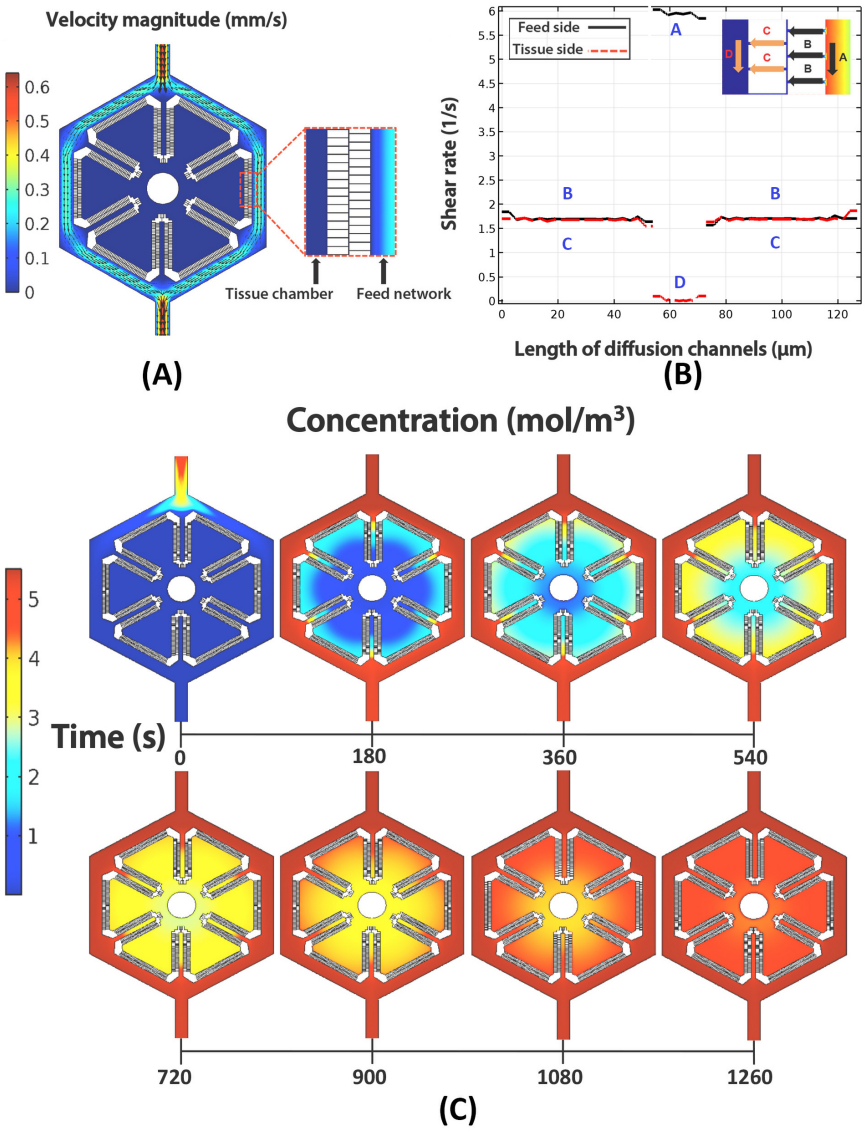

Figure 5.3: The simulation of the flow rates in the main feed network of a single liver lobule chamber is shown with an inlet flow rate of 1 μl min^{-1} (A). Flow velocity drops significantly inside the chambers compared to the feed network. The shear rate has been shown in graph (B). Shear rate in region A, the feed network, is the highest and in region D, inside the chambers is negligible. Diffusion of glucose ($D = 9 \times 10^{-10}$ m^2 s^{-1}) into the cell culture area was simulated under the introduced velocity field (C).

provide a low-cost option for feature sizes typically with the critical dimensions around 5-10 μm, whereas, chromium masks can achieve structures with sub-micron resolutions [141].

SU8 is a negative epoxy photoresist, which was initially developed in IBM labs [142]. It has been used widely in microfluidic fabrication due to relatively easy processing steps and the ability to produce high aspect ratio structures with a broad thickness variety from hundreds of nanometers to hundreds of microns.

The SU8 resist is photosensitive in the i-line (λ=365 nm) region and after ultraviolet (UV) exposure through the photomask is developed and further processed to yield the microfluidic masters. For complex or multilayer structure fabrication a mask aligner is required to adjust and align the features on subsequent layers. However, single-layer microchannels can be easily fabricated using a basic broadband UV lamp and plastic transparency masks.

In my work, I used silicon wafers as the substrate for constructing microfluidic patterns. Typically, the fabrication process started with cleaning the silicon wafers with a simple solvent-clean protocol. Wafers were immersed in acetone, methanol and isopropyl alcohol (IPA) and dried with nitrogen pressure gun. The cleaning step yielded a spotless surface for photoresist coating by removing dust, oil and organic residues.

4-inlet microfluidic chamber

For fabrication of the systems we used 3-inch <100> double-side polished silicon wafers as substrate. SU8-2015 (MicroChem Corp., Newton, MA, USA) was spin-coated at 1500 rpm to create structures with the height feature of 27 μm. Wafers underwent a soft bake step at 65°C for 2 min and 95°C for 5 minuets. After photolithography process using MA6 mask aligner (Suss MicroTec, Germany) wafers were post exposure baked (PEB) at 65°C and 95°C for 3 and 10 min respectively. Afterwards wafers were developed in mr-Dev 600 (microchem, Germany) and rinsed with IPA. The finished wafers were used as SU8 masters for fabrication of devices in PDMS.

Figure 5.4 illustrates the photolithography and PDMS molding steps to fabricate the 4-inlet device.

The design of the 4-inlet system was slightly modified by adding alignment marks and inlet-outlet nodes to the original design to fit a brass frame and punching needles as shown in figure 5.5(A). A brass ring was then fitted on the wafer using the alignment marks. The lid for the ring carried the punching needles and a central opening to cast PDMS on the wafers (figure 5.5(B) and (C)).
To make the devices, I prepared the PDMS mixture with a ratio of 10:1 PDMS:crosslinker **(papers I, II and III)**. After preparing the PDMS mixture and degassing in a vacuum desiccator (Item Z119016, Sigma-Aldrich, Germany) for around 30 min, the mixture was casted on silicon masters and cured in a conventional oven at 90°C for 2-6 hours. PDMS replicas were then peeled off, rinsed with IPA and ethanol and permanently bonded on microscope glass slides (Menzel #1 , VWR, SWEDEN) by air plasma treatment (PDC-32G/32G-2 (115/230V), Harrick Plasma, Ithaca, NY, USA) for 30 seconds.

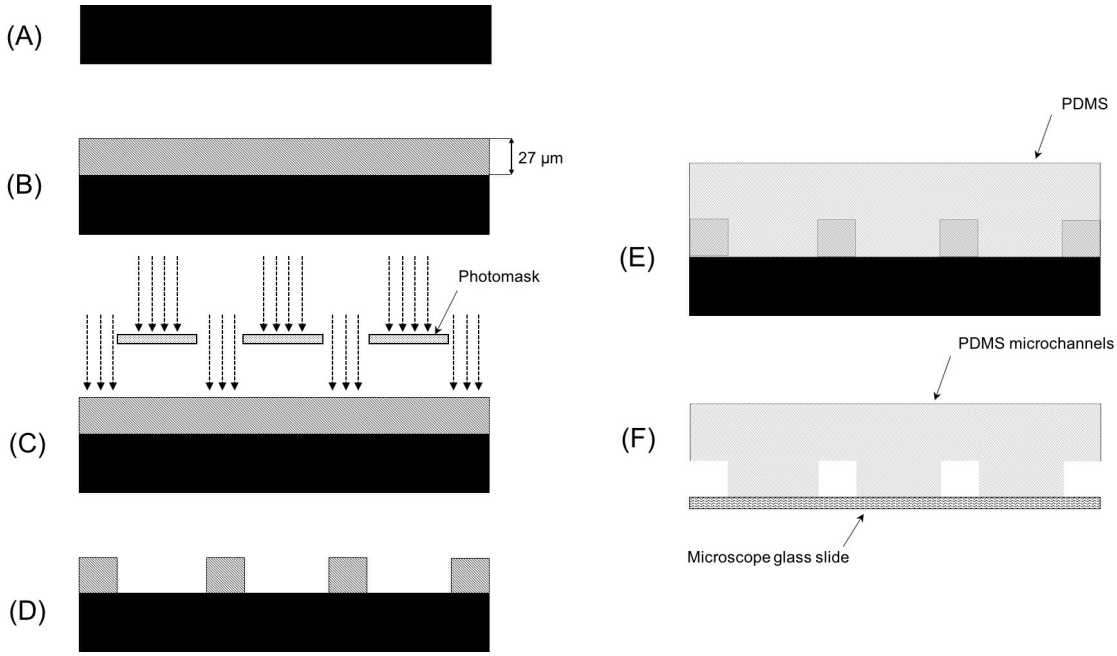

Figure 5.4: To fabricate a single-layer SU8 master with the height of 27 μm, the photoresist was spin-coated (B) on the silicon wafers (A) at 1500 rpm. After UV exposure (C) and developing step in mr-Dev 600 developer (D), SU8 masters were casted with PDMS (E). The crosslinked polymer was peeled off the wafers and permanently bonded on the glass slides by air plasma surface treatment (F).

CellComb device

To fabricate the CellComb device SU8-5 was spin-coated at the speed of 3000 rpm for 30 seconds on 3-inch <100> silicon wafers and processed accordingly. Soft bake times were similar to the 4-inlet device, however, PEB periods were adjusted to 1 and 3 min at 65°C and 95°C respectively. This fabrication protocol resulted in microchannels with the height profile of 5 μm and minimum feature size of 2 μm at the V-pockets. Similar steps were followed with SU8-25 for the mammalian cell device with the height adjusted to 15 μm.

Figure 5.6 shows an illustration of the photolithography and PDMS molding steps to fabricate the CellComb device. Fabrication of the microfluidic PDMS replicas followed the same steps as explained for the 4-inlet device.

VLSLL device

Fabrication of VLSLL device followed a multilayer coat-bake protocol. Cell culture layer and seed-feed network were fabricated in separate steps. To create the cell culture layer, the first step was to fabricate the diffusion passages. SU8-2002 was

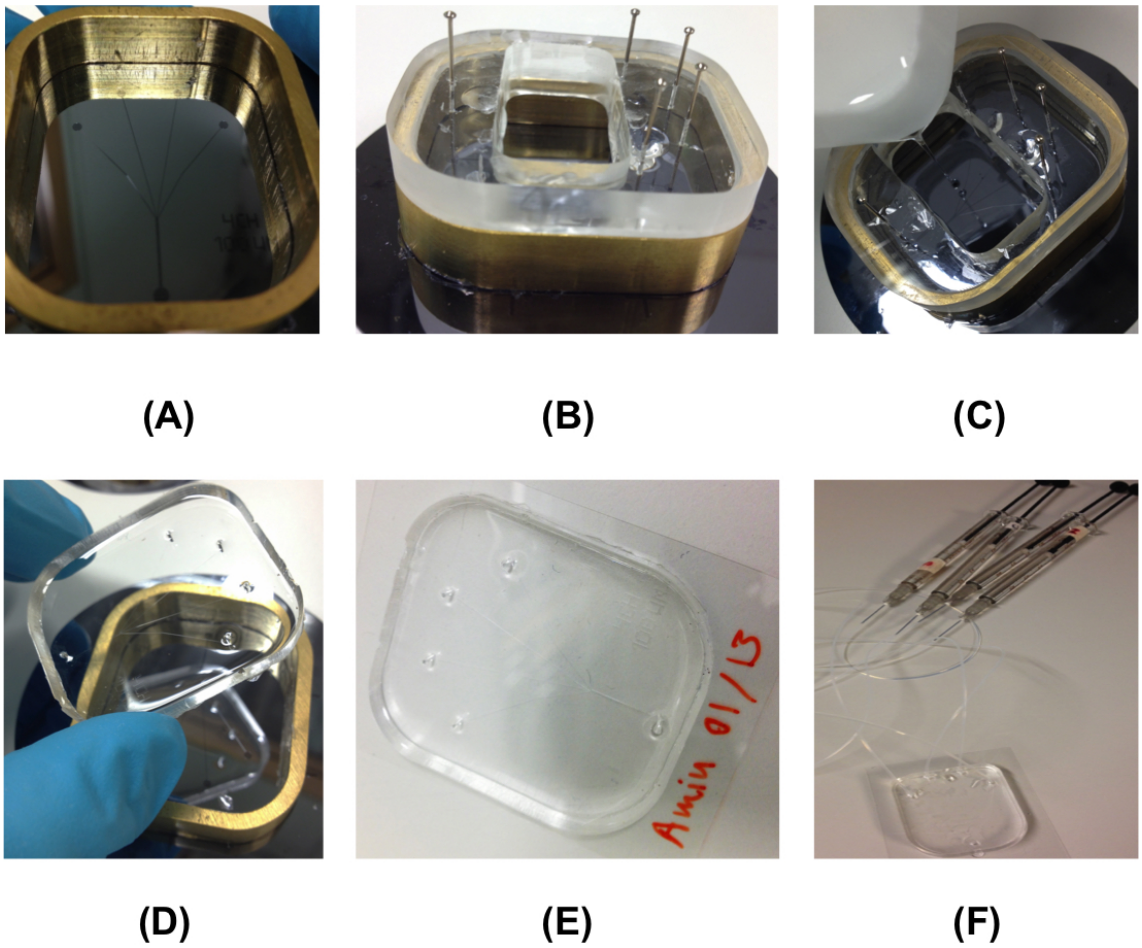

Figure 5.5: A brass ring (A) was custom-made and aligned on the masters to carry the PDMS lid and punching needles (B). After PDMS casting and bonding (C-E), microfluidic devices were ready for attaching the syringes and tubing (F).

spin-coated on 4-inch <100> wafers as shown in figure 5.7(A). After the lithography process wafers were developed and hard baked at 160°C for 10 min. Subsequently, the processed wafer was coated with SU8-2035 to create the 60-μm media circulation channels and honeycomb cell culture chambers (figure 5.7(B)). After UV exposure and PEB steps the wafer was stored at room temperature for at least 24 hours for rehydration without going through the development step. At the next step wafers were coated multiple times with SU8-2035 to yield a 400-μm thick stencil layer to readily pierce the central apertures in the PDMS cell culture chambers. To facilitate the chemical and mechanical stability of the multilayer coating, a soft bake step of 10 min at 65°C and 25 min at 95°C was performed in between each coating. After the last coating step wafers were UV exposed and left for 24 hours. All layers were eventually developed in a single step. The top layer containing the seed-feed network

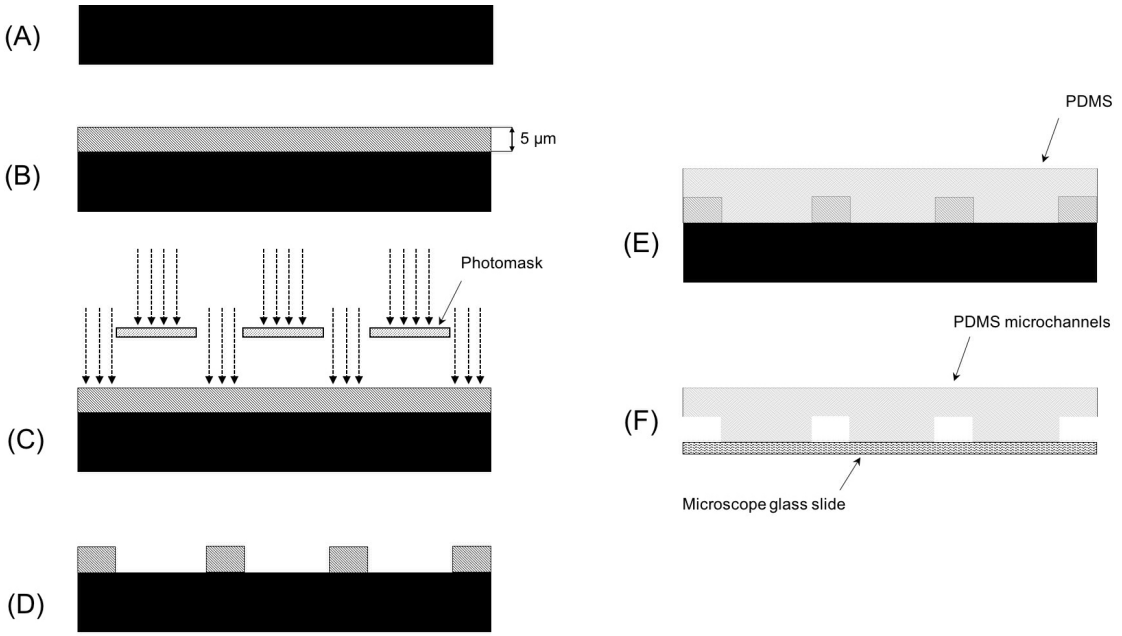

Figure 5.6: Fabrication of CellComb device was similar to the 4-inlet microfluidics. The height of the device was adjusted for the average diameter of a yeast cell (5 μm) and the critical dimension of 2 μm. Hence SU8-5 was used for the SU8 master fabrication. The photolithography steps and PDMS channel bonding are shown in (A-F)

was fabricated in a single photolithography step, see figure (5.8).

To prepare PDMS replicas of the VLSLL devices, PDMS for the thin layer, containing the cell culture chambers and bottom fluidic network, was mixed in a ratio of 5:1 and spin-coated at 200 rpm for 45 seconds on the silicon wafers as seen in figure 5.7(J). To fabricate the top seed-feed network silicon masters were casted with a PDMS mixture of 15:1 ratio. This combination facilitated a strong PDMS-PDMS bonding between the two layers [143] and prevented leakage during long-term cell experiments. Final devices (figure 5.8(G)) were rinsed with ethanol after bonding and dried in the oven overnight. A sterilization with oxygen plasma (BenchTop RIE (O2), Plasma-Therm, USA) was carried out at 100 W for 5-7 min. Devices were then vacuum sealed and stored at room temperature.

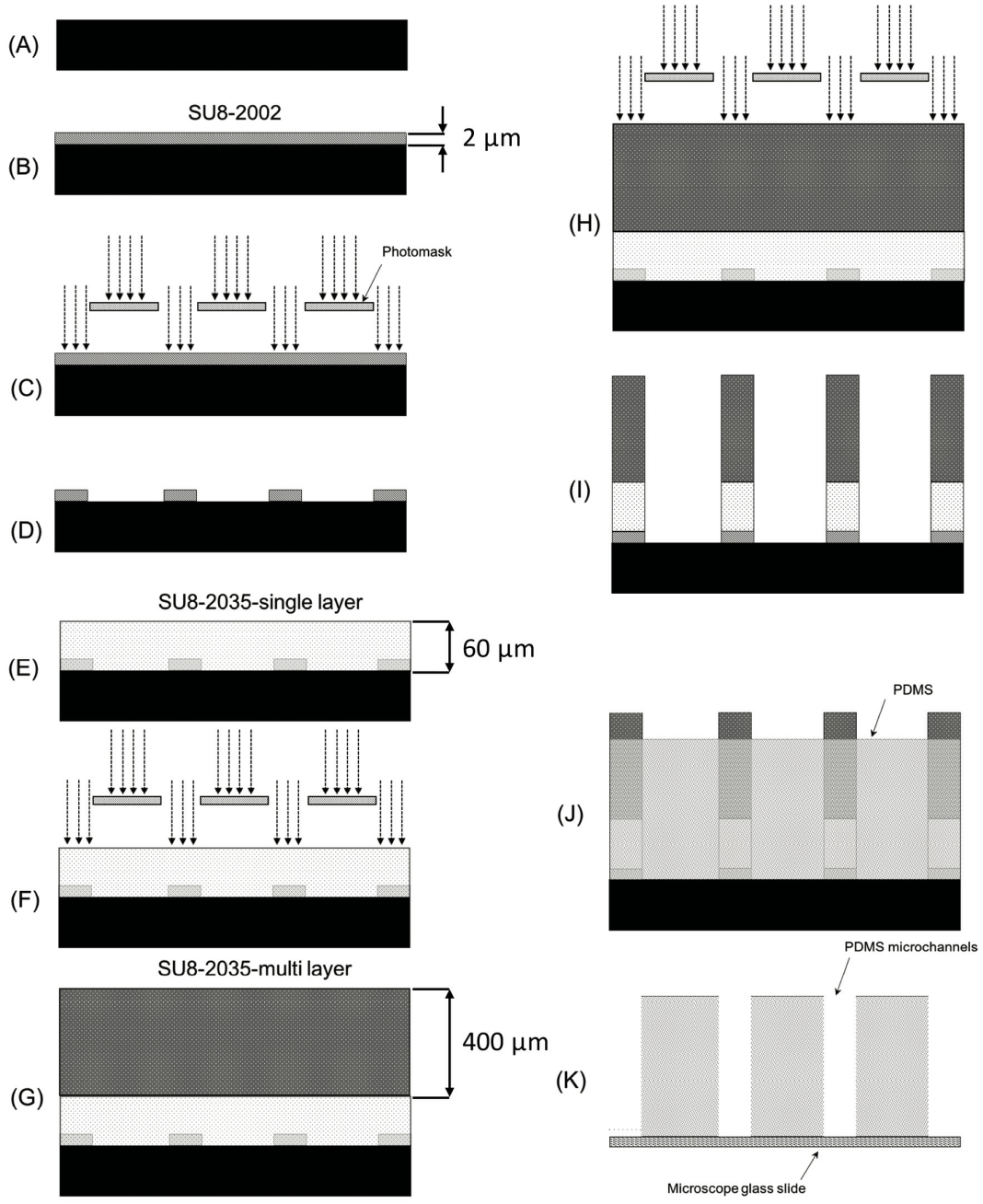

Figure 5.7: The VLSLL device comprised two layers of PDMS bonded on top of each other. The cell culture chambers were incorporated in the thin bottom layer while a separate seed feed network was fabricated. The SU8 master for the thin layer was fabricated in a multi-coat approach and the features were developed simultaneously. The fabrication steps for the cell culture chambers are shown in (A-K).

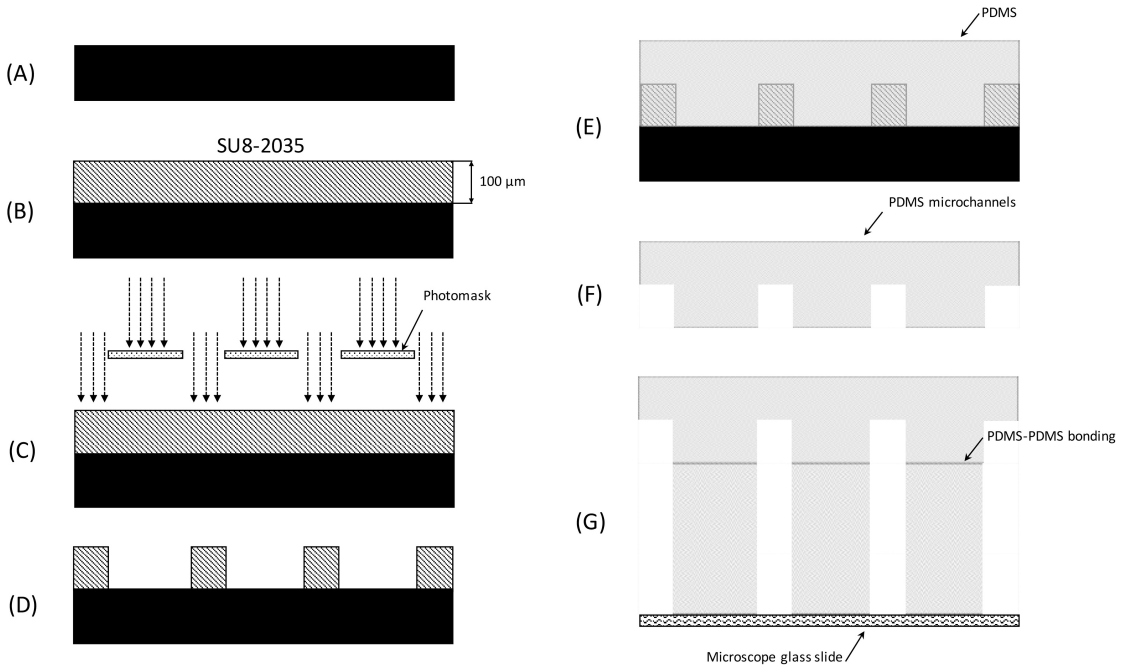

Figure 5.8: The SU8 master for the top layer was fabricated separately. The single-layer fabrication steps were followed (A-F) and the height of the device was adjusted to 100 μm. The top layer was eventually bonded by air plasma on the thin bottom layer (G).

5.2.2 Integration of optical tweezers with epi-fluorescence microscopy

In our studies we used an optical tweezers set up (see figure 5.9) as described in the previous published work [81, 82, 144]. A single infrared 1070 nm laser beam was focused through a 100× oil immersion objective (Leica Microsystems) with NA=1.3. The output power of the laser was set to 400 mW on the laser control box which attenuated in the optical pass and measured as 240 mW on the sample plane. Trapping time for each cell was kept under 10 seconds previously optimized [145] to maintain cell viability and minimize the photodamage to the cells.

Epi-fluorescence microscope stage (DMI 6000B, Leica Microsystems, Wetzlar, Germany) was used to acquire all the fluorescent time-lapse images. The stage was equipped with a broadband halogen lamp (Leica Microsystems, Wetzlar, Germany) that was set to minimum output power (10 μW) to prevent photobleaching of the dyes and provided the excitation light for green, red and blue fulorophores. Confocal microscopy was carried out in the microscope stage (LSM 700, Zeiss, Germany) at CCI facilities, University of Gothenburg.

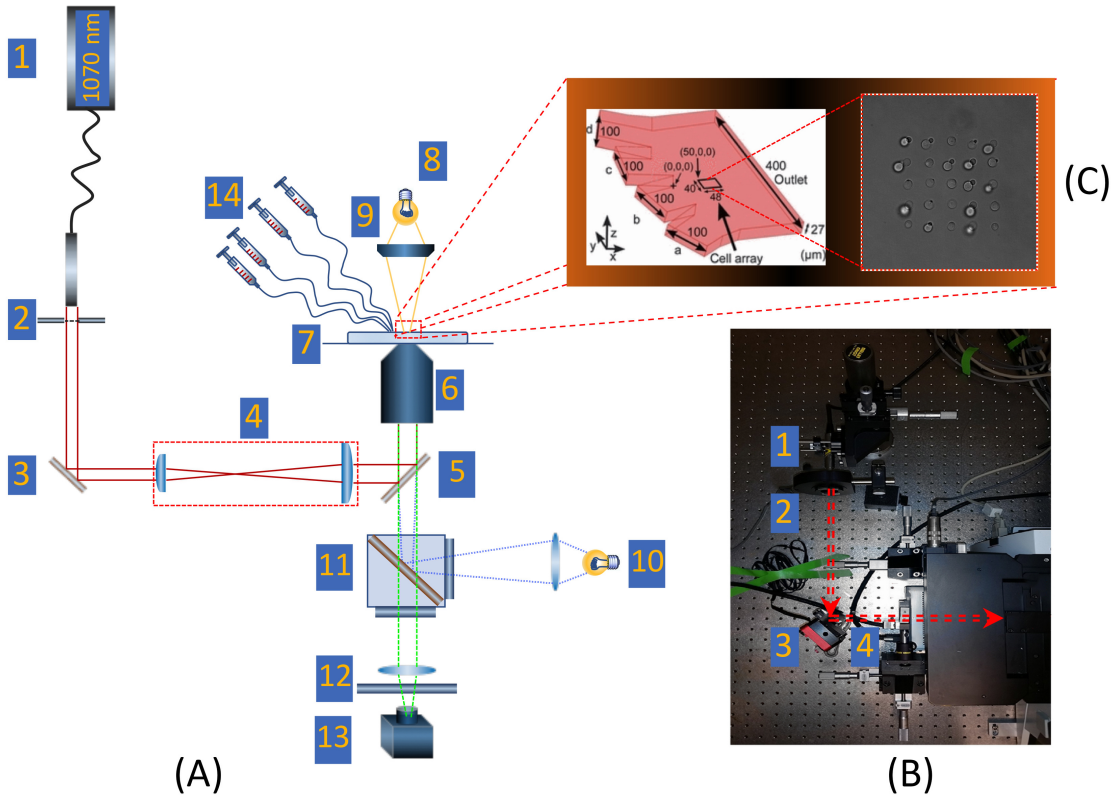

Figure 5.9: This figure (A) shows the drawing of integration of the infrared (1070 nm) laser (1) with the epi-fluorescence microscope stage. The laser light passes through a manually controlled shutter (2). The gimbal mounted mirror (GMM) (3) in a 90° angle guides the laser to the beam expansion telescope (4). Through a dichroic mirror (5) the laser passes through a high NA = 1.3 objective (6) and gets focused on the sample plane (7). For brightfield imaging sample is illuminated by the microscope lamp (8) through the condenser (9). To acquire fluorescent images of the cells as described in chapter 3 (figure 3.2), the sample is illuminated by a halogen lamp (10) and through the optical path (11-12) the sample emission signal is collected and detected in the EMCCD camera (13). Syringes and the tubing is connected to the microfluidic device for sample handling (14). The components of the setup are marked in the picture of the optical table (B) with corresponding numbering labels. (C) shows the 4-inlet microfluidic chamber and immobilized yeast cells.

5.2.3 Cell preparation

Saccharomyces cerevisiae **(yeast cell)**

Yeast cell strain HSP104-GFP (BY4741 HSP104-GFP-HIS3-MX6) (Invitrogen) was used to run the experiments in this thesis. Cells were cultured at 30°C on a cell shaker (220 rpm) in synthetic complete (SC) medium, 0.67% yeast nitrogen base

(YNB) and 2% glucose supplemented with auxotrophic requirements. Prior to the experiments cell density was measured by a spectrophotometer (biochrom, Cambridge, England) and cells were collected at optical density (OD_{600})= 0.5-1.0.

NIH/3T3

NIH/3T3 mouse embryonic fibroblast cells were cultured in DMEM high glucose, 4mM L-glutamine cell culture medium (Gibco, ThermoFisher Scientific), 10% (bovine calf serum) BCS (ThermoFisher Scientific) and 1% (penicyline-streptomycin) PEST (ThermoFisher Scientific). Cells were cultured in 75 cm^2 flasks (Sarstedt, Germany) for 3-4 days to 60-80% confluency. Afterwards cells were passaged and prepared for the experiments by trypsin/EDTA (GE healthcare) treatment.

HepG2

HepG2 cells were purchased from Sigma Aldrich, Germany. Cryopreserved vials were thawed in 37°C water bath for 2 min prior to the experiments. Afterwards cells were transferred to pre-warmed RPMI 1640 (1X) GLUTAMAX^{TM} cell culture medium (Gibco, ThermoFisher Scientific), 10% (fetal bovine serum) FBS (Hyclone Thermo Scientific), 1% PEST (Hyclone, Thermo Scientific) and cultured in a cell incubator at 37°C with 5% CO_2. Cells were cultured in 75 cm^2 flasks (Sarstedt, Germany) for 4 days to 80% confluency. At this stage cells were detached from the culture flasks using trypsin/EDTA, centrifuged at 200×g for 3 min and re-suspended in pre-warmed media. Desired numbers of cells (3-7×10^5) were seeded in the devices mixed with or without 20% mix of media/Geltrex®(ThermoFisher scientific) in a 1:1 ratio.

hiPSC-derived hepatocytes

Cryopreserved vials of hiPSC-derived hepatocytes were purchased from Cellular Dynamics International (CDI, USA). iCell hepatocytes 2.0 were thawed in 37°C water bath for 3 min prior to the experiments. The plating and maintenance media were prepared according to the manufacturer's protocol. 1.5 ml B27 supplement 50X (ThermoFisher Scientific), 20 ng ml^{-1} Oncostatin M (R&D Systems, Minneapolis, USA), 0.1 μM Dexamethasone (ThermoFisher Scientific), 25 μg ml^{-1} Gentamicin (ThermoFisher Scientific) and 1.5 ml iCell Hepatocytes 2.0 medium supplement (CDI) were added to RPMI 1640 (1X) GLUTAMAX^{TM} (Gibco, ThermoFisher Scientific) to prepare the plating medium. The thawed cell vial was transferred to 10 ml of pre-warmed plating medium. After a centrifuge step at 200×g for 3 min, cells were re-suspended and were ready to seed. Based on the protocol, 96 well plates (NUNC^{TM}) were coated with collagen I (Sigma Aldrich, Germany) in advance and seeded with a cell density of 3×10^5 cells cm^{-2}. Based on the experimental procedure, devices were either pre-coated with collagen I or cells were mixed with 20%

media/Geltrex^{TM} in a 1:1 ratio. After cell seeding, plates and devices were transferred to the incubator and a complete media change step was performed 4 hours later. Plating media was replaced on a daily basis until day 5. From day 5 plating media was replaced with maintenance media (plating media without Oncostatin M) and changed every other day.

5.2.4 Cell seeding and microfluidic device operation

4-inlet microfluidic chamber

To immobilize yeast cells in the 4-inlet devices, channels were treated with 1 mg ml^{-1} concanavalin A (ConA), 100 mM NaCl and 10 mM Tris/HCl for 30 min prior to the experiments. ConA solution was injected into all the channels and the device was gently flushed with the solution. Systems were rinsed with YNB afterwards and cell suspension as well as YNB, Hog1 inhibitor and sodium arsenite solutions were connected to the designated inlets (**paper I**). Syringe pumps (CMA 400, CMA Microdialysis, Solna, Sweden) were programmed to deliver the desired flow rates and controlled through a costume made automation in OpenLab software. Cells were flushed into the chamber, captured by the optical trap and pushed against the bottom of ConA-coated coverglass. ConA treatment enabled cell attachment on the bottom of the coverglass. The size of the cell array was determined in the software (5×5 cells). After cell-trapping step, cells were covered with the inhibitor or stress solution based on the experimental plan (**paper I**).

CellComb device

Cell capturing in the CellComb device was performed in a single step of constant flushing the cell inlet with the cell suspension (**papers II and III**). Cell loading step required less than a minute to accomplish which was a major advantage over the optical trapping technique. Single or multiple cells could be trapped inside the V-pockets controlled by the geometry of the system and cell density. The main channel of the device was rinsed with YNB after the cell-trapping step to flush out the non-trapped cells. Stress solutions were introduced to the system via the main or side inlets and imaging was performed. The device could be imaged in multiple sections (13 sections along the length of the device with 8 pockets in each section, fitted to the field of view of the camera) by moving the microscope stage.
The first step in operation of the CellComb with NIH/3T3 cells was aimed at successfully immobilizing the cells in the device. To achieve the single cell trapping, cells were detached from the culture flasks and resuspended in fresh cell medium after a centrifugation step. In **paper II** we explored the possibility of trapping cells in suspension with the same principle described for yeast cells. Although the cell

entrapment step was successfully conducted, further care was required to maintain the cells viable and functional.

VLSLL device

VLSLL device was tailored to facilitate long-term culture of human liver cells (**paper IV**). To start each experiment sterilized devices were placed in a vacuum desiccator at least 24 hours prior to cell seeding. This step aided the cell loading as air-liquid displacement inside the PDMS body provided a temporary suction effect inside the device. A negative pressure of 3 psi applied to the feeding inlet helped load the cells uniformly and achieve a packed population inside the culture chambers. Cell preparation as described in section 5.2.3 was performed accordingly based on the plating and maintenance protocols for HepG2 and hiPSC-derived hepatocytes. Special care was necessary in the cell seeding process to impose the least stress and damage to the cells. The hiPSC-derived hepatocytes were the most fragile after thawing and plating process was carried out as suggested by the provider (CDI). After cell seeding step devices were left in a no-flow condition to aid the cell adherence and stabilize the cultures. Cell culture media was connected to the feed inlets via microfluidic connectors and syringe pumps were programmed to 1 μl min^{-1} flow rates (**paper IV**). Devices were inspected for cell morphology and flow conditions with a light microscope (Olympus, CKX41, Japan).

5.2.5 Assay, buffer, and substance preparation

Hog1 inhibitor

We dissolved Hog1 inhibitor 4-(1-benzyl-4-phenyl-1H-1,2,3-triazol-5-yl)-N-isopropylpyridin-2-amine (M = 478.67 g mol^{-1}) in dimethylsulfoxide (DMSO) [146]. The concentration of stock solution was 1.9 mM and diluted in YNB on the day of experiments to the final concentration of 10 μM.

Sodium arsenite ($NaAsO_2$)

Sodium arsenite ($NaAsO_2$) (Sigma Aldrich, Germany) was fresh prepared on the day of experiment (dissolved in Mili-Q water) and brought to the final concentrations of 0.1, and 0.5 mM (**paper I**) and 0.5 mM (**paper III**).

Fluorescein solution

Uranine (disodium salt form) was dissolved in Mili-Q water and a final concentration of 0.2 mM fluorescein (green fluorescent dye) solution was prepared (**paper II**).

ELISA

Human albumin ELISA kit (Bethyl laboratories, Montgomery, TX) was used to measure the albumin secreted by hepatocytes both in the devices and 96 wells. Based on the manufacturer's protocol clear 96 wells (NUNC^{TM}) were coated with the coating antibody mixed in coating buffer. Wells were then washed, and blocking solution was added. After sample dilution in the sample-conjugate buffer and incubation at room temperature, detection antibody was added to the wells. Ready-to-use TMB solution was added to each well to create the luminescence. The reaction was stopped by adding the stop solution and wells were measured in a microtiter plate reader (FLUOstar Omega, BMG LABTECH, Germany) at 450 nm wavelength in absorbance mode.

Urea assay

Urea synthesis by hepatocytes was measured by an enzyme reaction urea assay kit (Sigma Aldrich, Germany). Samples were diluted in urea assay buffer, and added to 96 wells (NUNC^{TM}). The reaction mix including the enzyme mix, the developer, the converting enzyme and the peroxidase solution was prepared according to the manufacturer's protocol. After carefully adding the reaction mix to the samples, plates were incubated at 37°C for 60 min and measured at 570 nm in absorbance mode.

Cell viability Live/Dead® kit

Mammalian cell viability kit was purchased from ThermoFisher Scientific. Calcein AM was used to detect viable cells based on the esterase activity of the cells. Live cells cleave the calcein AM dye by the intercellular esterases and turn it to a green fluorescent probe. Ethedium homodimer-1 (Ethd-1) is a red fluorescent dye that passes through the damaged cell membranes and binds to the DNA of apoptotic or necrotic cells. Calcein AM and ethidium homodimer-1 (Ethd-1) were prepared fresh in PBS (-Ca, -Mg) to the final concentrations of 4-6 μM before every staining. 96 wells and microfluidic devices were washed prior to the staining with PBS. Cells were incubated with the dyes at 37°C for periods between 30-90 min (**paper IV**). After another wash step cells were imaged using the epi-fluorescence or confocal microscope stage.

Hoechst dye for cell nuclei staining

Hoechst 33342 fluorescent stain (20 mM, item 62249) was purchased from ThermoFisher Scientific. Hoechst is a blue florescent dye that binds to DNA with high affinity and without interacting with the nucleic acids. The dye is highly cell permeable and is commonly used to stain the nuclei of eukaryotic cells. Upon exposure

it provides a distinct blue fluorescence signal at 460 - 490 nm. The fluorescent dye was prepared fresh before each staining and was diluted to the final concentration of 10 μg ml^{-1} in PBS (-Ca, -Mg). Incubation time was between 10-30 min.

CDFDA for bile canaliculi staining

CDFDA (5-and-6)-carboxy-2',7',-dichlorofluorescein diacetate (Sigma Aldrich, Germany) was used to stain the hepatocytes for formation of bile canaliculi network. By means of intercellular esterase activity, hepatocytes cleave CDFDA dye. Upon staining, the cleaved dye loses the diacetate part and is then transported out of the cytoplasm into the canaliculi network in between the adjacent cells with involvement of MRP2 transporters [123]. Final concentration of 10 μM was prepared fresh before each staining and incubation time set to 10-15 min at 37°C.

5.3 Data analysis

To analyze the results obtained from the experiments in **papers I-IV**, the data was processed in image analysis softwares for the brightfield and fluorescence microscopy images. For yeast cells the imaging data was analyzed to quantify the number of Hsp104-GFP aggregates under different experimental scenarios. For experiments with the liver cells, live cell staining fluorescent data was obtained and used to assess cell integrity and formation of multi-layer cell structures in the microfluidic devices.

Image analysis

In **papers I, II and III** the acquisition of the data was handled by Openlab software. Time-lapse images of the cells in brightfield and fluorescence mode were taken in series of stacks along the z axis for each time point and every field of view. The separation between the stacks was decided based on control experiments and trial runs. Typically we acquired 7-10 images for yeast cells with the z-slice spacing between 0.6-0.9 μm. The fluorescent data from each image series was overlaid with the brightfield images and analyzed in a custom-made image analysis software, CellStress [147]. To identify the outline of the cells, the algorithm for cell contour recognition in the software CellStat [148] was used jointly with CellStress. The fluorescent data was analyzed based on the intensity of the signal from each z-slice and the intensity points found in the layer. This way we could automatically obtain the number of total aggregates in each cell. The results of the analysis round were manually controlled to avoid false aggregate count. To analyze the fluorescence microscopy data acquired from staining of liver cells, software ImageJ (https://imagej.nih.gov/ij/) was used extensively to separate color channels and overlay stained layers with calcein AM, hoechst 33342, Ethd-1 and CDFDA.

Plate-based assay data analysis

To analyze the ELISA and urea assay measurements in **paper IV**, a series of sample dilutions were performed to maintain the read out of the sample absorbance in the linear range of the standard curves of the assays.

ELISA analysis

The ELISA kit was optimized to detect human albumin in the serum with a standard curve obtained for a dilution series of 6.25 - 400 ng ml^{-1}. In each absorbance measurement run with sample and standard duplicates, results were monitored for the duplicates to be within a 10% range from each other. Each assay was repeated at least 2 to 4 times to ensure the consistency of the results. The standard curve for each measurement was prepared by subtracting the blank values from the average of duplicate standard concentrations. The new values were plotted against the corresponding albumin concentrations from the assay. The standard curve was obtained by applying a 4 parameter logistic regression curve-fitting. The concentration of unknown samples were found by correlating the average absorbance values to the standard concentrations. The sample dilution factors were applied to obtain corrected albumin values. The results were then corrected for the number of seeded cells in each device or 96 well and the period of time the cell supernatant was collected. Final results were presented as the amount of albumin in $ng/h/10^6$ cells as seen in figure 6.6(A) and figure 6.7(A).

Urea analysis

Urea assay is an enzyme reaction assay that results in a final reaction product which, through colorimetric absorbance measurement is correlated to the amount of urea synthesized by the hepatocytes. All the precautions taken with the ELISA measurements were repeated in terms of assay repetition and data consistency with the urea samples. The steps in preparation of the standard curve were the same and only the fitting algorithm was changed to the linear least square regression model. Results of measurements were corrected for the dilution factors, cell numbers and period of the supernatant collection shown in $ng/h/10^6$ cells as seen in figure 6.6(B) and figure 6.7(B).

Chapter 6

Summary of results

This chapter summarizes the experimental results in the appended papers.

6.1 Paper I: Microfluidic chamber in combination with optical tweezers to study uptake of sodium arsenite in single yeast cells

In **paper I**, we took advantage of an integrated experimental set up including an epi-fluorescence microscope and a single beam ($\lambda = 1070$ nm) infrared optical tweezers setup. In this study we conducted the induction and regulation of uptake of sodium arsenite in yeast in presence of glucose, mediated by a Hog1 inhibitor. We used GFP-tagged Hsp104 as the readout for arsenite uptake by the cells.

Various concentrations (5-25 μM) and incubation times (5-45 min) of the Hog1 inhibitor were introduced to the cell environment to eliminate the risk of false aggregate formation readouts induced by the inhibitor.

The final concentration of 10 μM and pre-incubation time of 5 min were selected for the inhibitor.

Compared to the control experiments with only YNB, exposing cells to 0.1 mM and 0.5 mM solutions of arsenite resulted in time- and concentration dependent increase in the formation of Hsp104-GFP protein foci, which, was attributed to the increase in concentration of arsenite in the cytosol. After 40 min of continuous arsenite exposure, around 50 % of the cells showed 2-4 aggregates per cell.

In the next step we pre-incubated the cell arrays with the Hog1 inhibitor for 5 min and introduced 0.1 mM arsenite solution into the chamber for an additional 45 min time period.

Our results as shown in figure 6.1 clearly showed that both the maximum number of aggregates per cell (nine aggregates) as well as the proportion of cells with aggregates (80 %) increased compared to the arsenite-only scenario.

Figure 6.1(A) shows the cells at the final time point of the experiments (45 min) for As (III)-only treatment whereas figure 6.1(B) shows the cells treated with 10

μM of Hog1 inhibitor for 5 min prior to arsenite exposure. As seen in figure 6.1(C) and (D) the number of aggregates in total and per cell, as well as the proportion of the cells showing aggregates indicate a significant increase with inhibitor treatment. This can also be seen in the number of the aggregates formed after 45 min under the two experimental conditions in the box plot in figure 6.1(E). The significance between the two data sets found using one-way ANOVA test ($* = p < 0.05$).

The mechanism behind the significant role of the Hog1 inhibitor in increasing the uptake of As (III) and hence damaged protein sites can possibly be explained with a hypothesis where the kinase activity of Hog1 is disabled in presence of the inhibitor compound. When cells are exposed to As (III) without the inhibitor treatment, phosphorylation of Hog1 via down-regulation of Fps1, through phosphorylation of Fps1, leads to drop in the uptake of arsenite. However, treatment with the Hog1 inhibitor, as seen in figure 6.2 results in the impairment of down-regulation of Fps1 by Hog1 and therefore increase in the uptake of As (III) via Fps1. Based on this model we could explain the increase in the number of protein foci with Hog1 inhibitor pre-incubation.

Additionally, we observed an earlier aggregate appearance in Hog1 inhibitor and arsenite co-administered cells. Benefiting from the single-cell analysis approach we analyzed the response of mother and daughter cells (buds), that were attached to the mother cells at the time of experiments. The cell-cell heterogeneity from varying cell cycles among the mature cells and the buds confirmed a distinct pattern in our data. Our results depicted in a box plot with the average number of aggregates at 45 min, in figure 6.3 showed that mother cells accumulated more protein damaged sites compared to the young buds during the course of treatment with both inhibitor and arsenite. Whereas, in the arsenite-only scenario no significant differences were observed between the mothers and fresh buds.

6.2 Paper II: Design and fabrication of a high-throughput microfluidic device for single-cell capture, exposure and imaging

In **paper II** I designed and fabricated a high-throughput multi-inlet microfluidic device for hydrodynamic trapping of single cells inside the V-shaped traps. This paper addresses the need for application-specific and high-precision tools to collect data for statistical analysis. We demonstrated that with an easy-to-operate microfluidic device (CellComb) it is possible to immobilize individual or groups of cells in PDMS blocks arranged in V-shaped placement. Via formation of high-velocity nodes at the nibs of the traps cells were dragged into the pockets and maintained with the stream of the flow. COMSOL simulations confirmed the formation of high jet flows exiting the traps into the two wider adjacent channels. Due to the increase of the flow resistance in the filled pockets, the high velocity region of the device

moved along the microchannels. Cell trapping procedure was performed using a syringe pump. The device could be effectively loaded with fast flushing the pump for 30-60 s. The device was designed to allow for cellular microenvironment perturbations with various substances. Full coverage of the cells in the main channel as well as local exposure from the side channels was shown. Trapping individual yeast cells and NIH/3T3 embryonic mouse fibroblast cells were achieved with tailoring the geometry of the device to the average size of each cell type (around 13-15 μm for NIT/3T3 cells measured on acquired microscope images). The single-block CellComb device could accommodate up to 6 yeast cells in each trap and total number of 624 cells in a completely filled device while maintaining the single-cell possibilities. The capability of the device in administration of extracellular perturbations was demonstrated with 0.2 mM fluorescein solution. We also demonstrated that the device could be operated in a comparatively low flow rate regime (nl min^{-1}) with stable cell immobilization and exposure.

6.3 Paper III: Effect of flow rate variation on formation of Hsp104 foci in yeast cells using the CellComb device

In **paper III** we used the principle developed in **paper II** for hydrodynamic capturing of yeast cells. The effect of flow rate dependency of Hsp104-GFP protein aggregate formation in single yeast cells was studied. Cells were diluted to the OD_{600}= 0.1-0.3 and seeded in the devices. We could achieve up to 80% trapping efficiency with multiple cells in each trap. Single-cell trapping efficiency of 60% was achieved for single-cell occupancy in each pocket. Controlling the initial cell density and preparing multiple dilutions was the only effort required to ensure a uniform cell loading without accumulating the microchannels with uncontrolled number of cells. Sodium arsenite was prepared at the final concentration of 0.5 mM to assure redistribution of Hsp104-GFP as confirmed in **paper I**. We observed a distinct heterogeneity in cellular responses under low (25 nl min^{-1}), moderate (50 nl min^{-1}) and high (100 nl min^{-1}) flow rates. Our data as seen in figure 6.4 showed a trend in formation of larger number of aggregates under the low flow rate compared to the high flow rate settings. We also observed the early appearance (15-20 min from the start of arsenite treatment) of Hsp104-GFP aggregates under 25 nl min^{-1} flow rate. Figure 6.5 shows the average number of aggregates per section of the device at 45 min under different As (III) flow rates compared to the non-treated (NT) cells. We attributed this increase in the uptake of the substance to the higher availability of the chemical in the cell proximity under low flow rates, leading to increased passive diffusion of As (III).

6.4 Paper IV: Long-term maintenance of HepG2 and hiPSC-derived hepatocytes in the VLSLL-on-a-chip device

In **paper IV**, a liver-on-a-chip device developed for drug metabolism studies in long-term *in vitro* cultures of liver cells was designed and evaluated. (VLSLL)-on-a-chip microfluidic device facilitated 3D tissue formation, long-term cultivation and monitoring of human hepatocytes. The two-layer culture and feed network configuration allowed for a compact and integrated device which, primarily was designed to be incorporate in modular multi-organ human-on-a-chip platforms. A single device comprised 18 hexagonal cell culture chambers mimicking the geometrical dimensions of the classic liver lobule. The diameter of the chambers varied between 1.2 - 2.4 mm.

In my experiments, devices were validated with HepG2 and hiPSC-derived hepatocytes. We operated the devices under two sets of experimental conditions for cell culturing.

The first set, were the experiments where I seeded the cells into the culture chambers without addition of ECM. Although this approach worked to a certain extent with the HepG2 cells, the hiPSC-hepatocytes demonstrated a limited adhering capability to the surface of the device and eventually lost viability. HepG2 cells on the other hand could be kept viable up to one week in culture with a significant decline of albumin secretion and urea synthesis from day 4 (Supplementary figure 3, **paper IV**).

The second set of experiments included using various forms of ECM involvement in the cell culture process. Devices were coated with rat tail-collagen I (Sigma Aldrich, Germany) prior to the experiments, or cells were mixed at the time of seeding with different concentrations of Geltrex® (0.15 mg ml^{-1}) or Geltrex™ (15 mg ml^{-1}). The second set of experiments revealed that any form of ECM addition to the culture system significantly improved the cell viability and resulted in longer maintenance of the cultures. HepG2 cells showed stable levels of albumin and urea for at least two weeks as seen in figure 6.6. hiPSC-hepatocytes could be maintained in culture for at least three weeks with collagen I coating as well as Geltrex™ mixing. Our results showed (see figure 6.7) that the levels of albumin in hiPSC-hepatocytes were significantly higher than the HepG2.

Urea synthesis was, however, higher in HepG2 cells, yet comparable in case of hiPSC-hepatocytes. As it has been published by Berger *et al* [149] levels of urea synthesis and functionality measures can significantly vary based on the donor variation of hiPSC-hepatocytes. Additionally, the different formulation of the culture media can contribute to different levels of urea synthesis. Another plausible argument could be cell proliferation in HepG2 after seeding and formation of 3D tumor structures while, the maturation process of iPSC to hepatocytes impairs the proliferation capability of hiPSC-hepatocytes. Therefore, proliferation of HepG2 cells

may effect the urea synthesis. Further experiments are required to validate either of these explanations possibly by using assays to monitor the proliferation of the cells.

To access the viability of HepG2 cells three molecular probes, calcein AM, Ethd-1 and hoechst were used. Figure 6.8 shows a confocal image of the HepG2 cells stained with the three dyes on day 2 in culture. The viability of the HepG2 was constantly monitored during the culture period (up to 14 days, **paper IV**, supplementary figure 2) and used in correspondence with the albumin and urea production as a measure of cell integrity.

To verify the formation of bile canaliculi in the cultures, hiPSC-hepatocytes were stained with CDFDA dye. We observed the formation of bile canaliculi networks only in the 3D cultures (figure 6.9(A)). The formation of bile canaliculi network in the interfaces of tissue-like structures was observed as shown in **paper IV** on day 8 and day 16 in the cultures. Monolayer cultures of hepatocytes showed an insignificant formation of bile canaliculi as seen in figure 6.9(B).

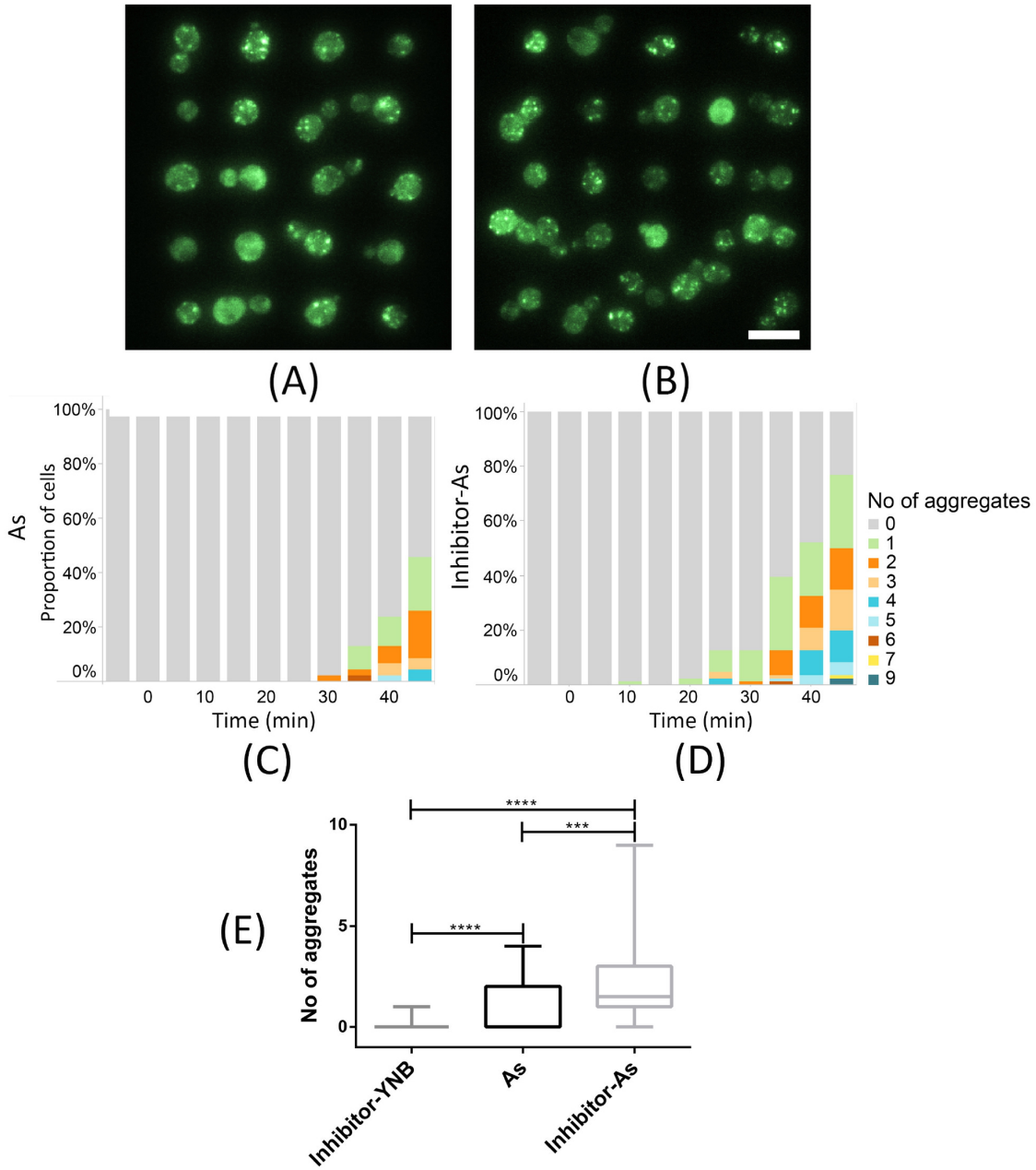

Figure 6.1: As (III) and Hog1 inhibitor co-administration in our experiments showed a significant increase in the arsenite uptake by the cells. (A) is the fluorescent image of an array of yeast cells subjected to 0.1 mM of sodium arsenite for 45 min. (B) shows the final time point of the experiment for the inhibitor pre-treatment scenario (Scale = 10 μm). The number of Hsp104-GFP aggregates in the arsenite-only scenario (C) significantly increased with the 5 min pre-incubation with the Hog1 inhibitor (D), shown for the percentage of all cells in the experiment. The average number of aggregates in the three scenarios of non-treated (NT), arsenite-only and inhibitor co-administration has been shown in the box plot denoting the significance of inhibitor treatment in Hsp104 redistribution. (*=$p < 0.05$)

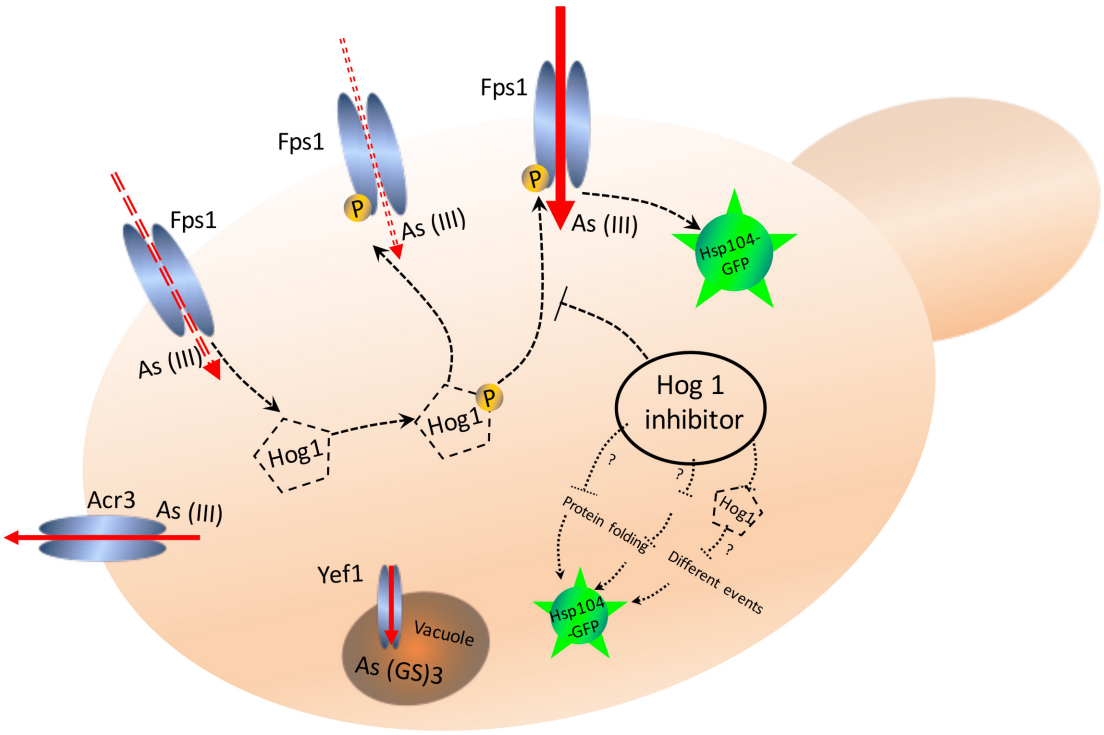

Figure 6.2: In our model for the uptake of As (III) we show that the port of entry of arsenite to the cell is through Fps1 channels and in case of no co-administration of the Hog1 inhibitor the compound gets transported out of the cell through Acr3 export pumps or enters the glutathione cycle. In presence of Hog1 inhibiter, the phosphorylation of Hog1 and therefore the activity of Fps1 gets impaired and concentration of arsenite increases in the cytosol resulting in the early appearance and elevation of the Hsp104-GFP foci with distinct fluorescent signal. Other possible scenarios such as involvement and activation of other kinase pathways are likely in mediation of Hog1 inhibitor and increase of the arsenite uptake by the cells, however, further experiments are required to assess these possibilities.

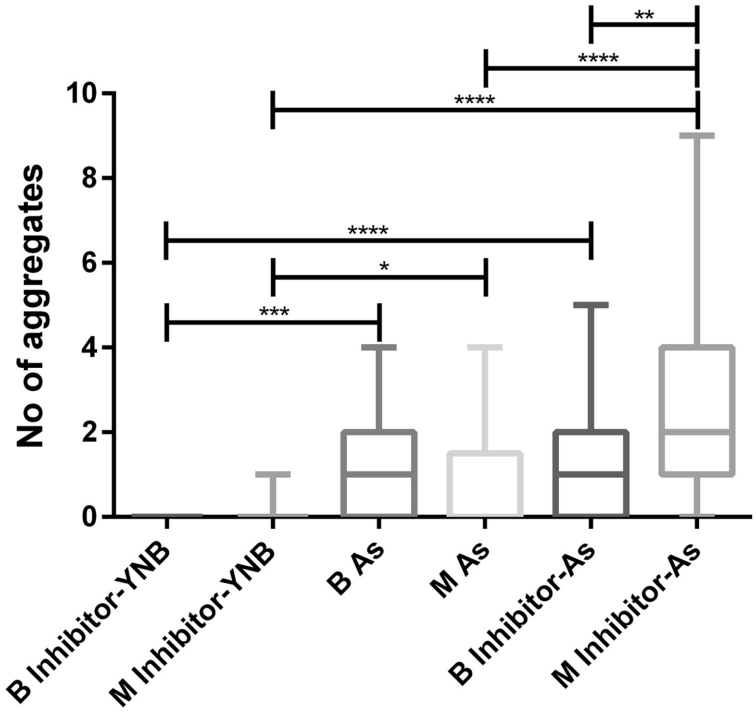

Figure 6.3: The number of aggregates in the cells is shown for the mother and daughter cells at the final time point of the experiments 45 min. We observed that mother cells accumulated significantly higher number of aggregates compared to the buds in the co-administration of Hog1 inhibitor and As scenario. This effect was not pronounced in the As-only treatment. Also we observed that the uptake of arsenite showed a larger significance in only mother cells under the two treatment scenarios. (*=$p < 0.05$)

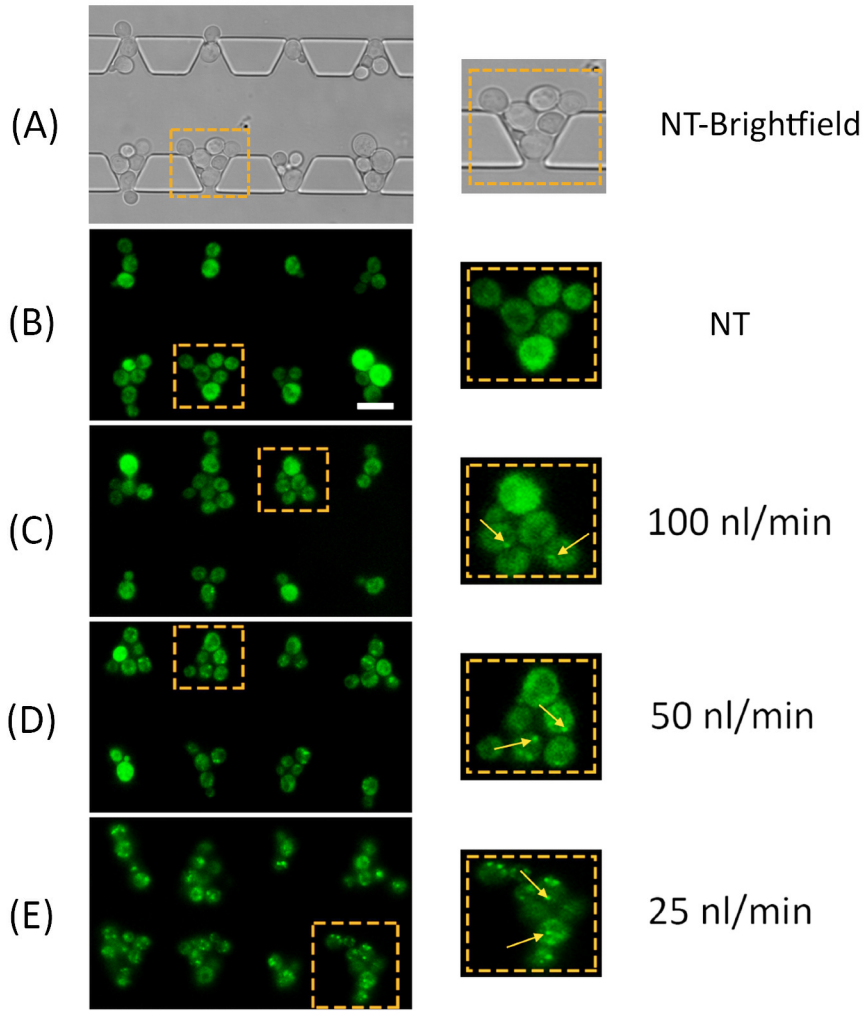

Figure 6.4: In the CellComb device, cells were subjected to three different flow rate scenarios. The device was operated under relatively small flow rates with the 100 nl min^{-1} marked as highest and 25 nl min^{-1} as the lowest flow rate. Cells were immobilized in the traps prior to treatments (A). Our data showed that number of aggregates increased with the decrease in the inlet flow rates (C-E) compared to the NT cells (B) (Scale = 10 μm). Arrows show the Hsp104 aggregates.

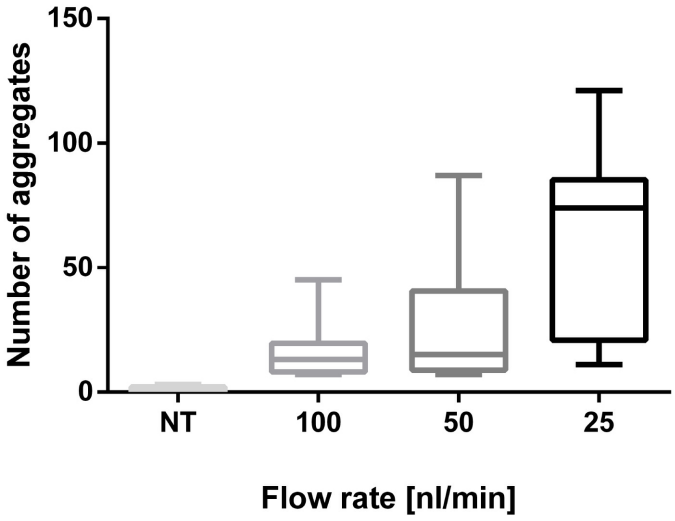

[nl min^{-1}]	NT	100	50	25
NT	-	****	****	****
100	****	-	**	***
50	****	**	-	***
25	****	***	***	-

Figure 6.5: The box plot shows the significance of the flow rate reduction on the Hsp104 relocalization. The average number of aggregates in each section of the device (field of view of the camera with 8 trap placements) was compared for different flow scenarios at final time point of 45 min. (*=$p < 0.05$).

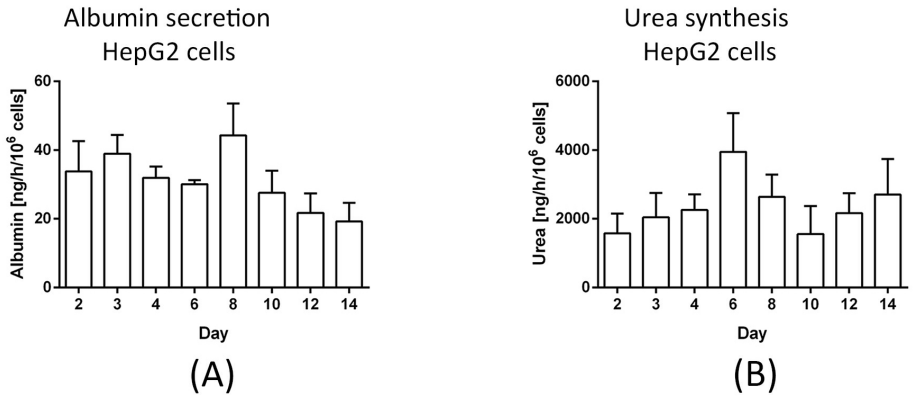

Figure 6.6: Secretion of protein albumin (A) and synthesis of urea (B) as liver-specific metabolic markers was monitored in the HepG2 cultures in the VLSLL device for 14 days. The cell suspension was seeded into the devices in a 1:1 v/v mixture with 20% diluted Geltrex® (0.15 mg ml^{-1}). Cultures showed sustained levels of albumin and urea production. Error bars show the standard deviation.

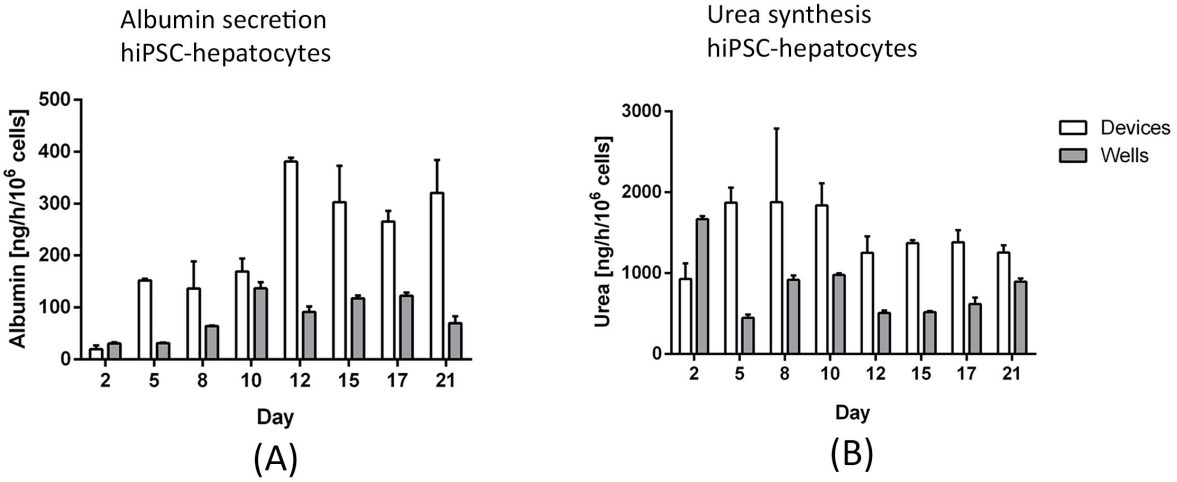

Figure 6.7: hiPSC-hepatocytes were seeded into 96 wells and devices pre-coated with collagen. The cell adhesion and viability was maintained on the gel-treated surfaces and devices as well as 96 well plates were measured for the amount of albumin and urea production. Both albumin secretion and urea synthesis were higher in the VLSLL devices compared to the 96 well plates under the time period of 21 days. (A) shows the comparison of albumin secretion between devices and 96 wells whereas (B) depicts the differences in urea synthesis. Error bars are the standard deviation.

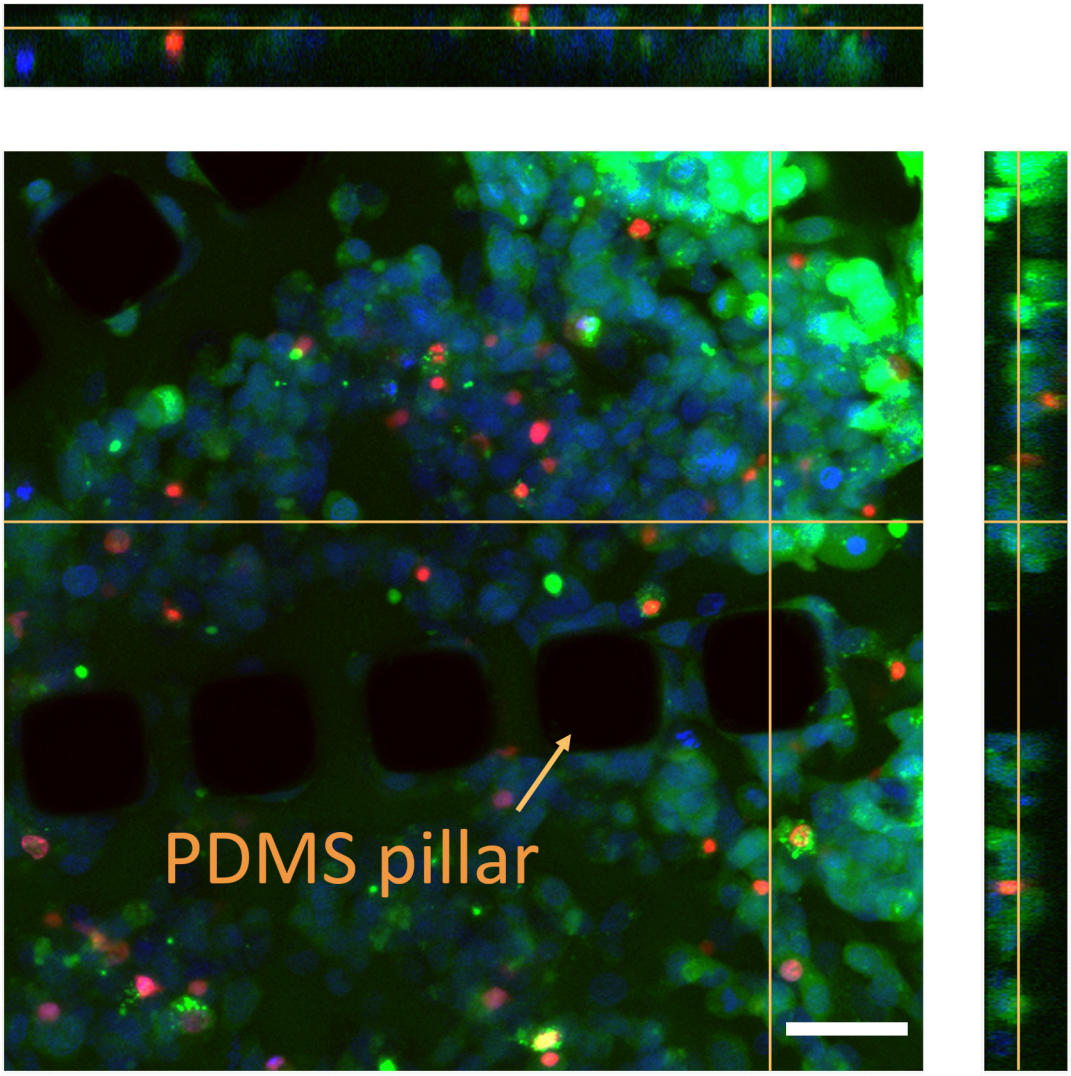

Figure 6.8: The confocal image of HepG2 cells in culture in the VLSLL device, 2 days after seeding. 30 stacks of images were taken with 2 μm split. Cells were stained with calcein AM (green, live cells), Ethd-1(red, dead cells) and hoechst (blue, cell nuclei). The images were taken in the center for cellular imaging (CCI), University of Gothenburg. (Scale = 50 μm)

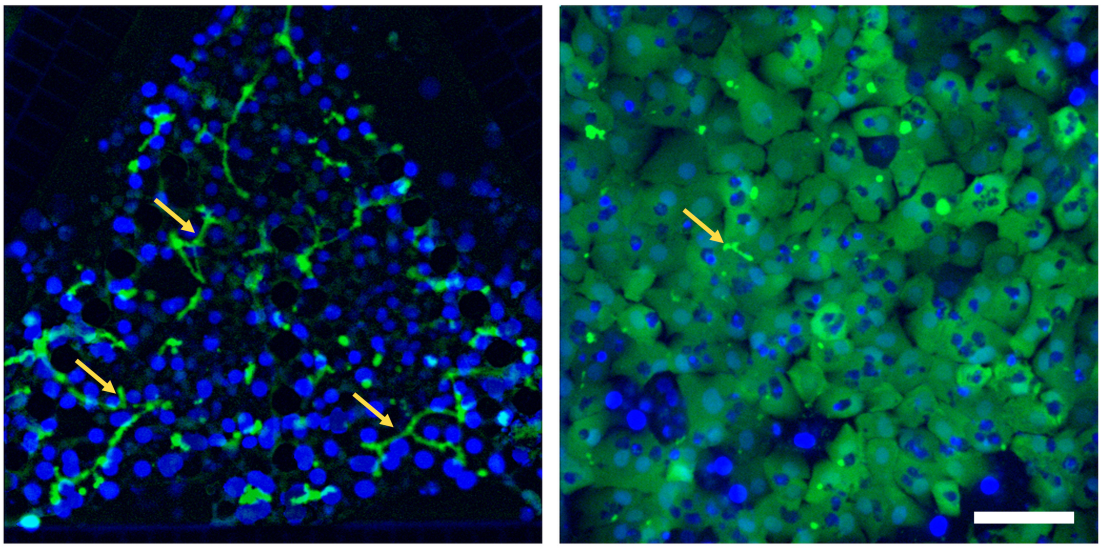

Figure 6.9: Exertion of bile is the hepatocyte-specific role in the liver. In our experiments we stained hiPSC-hepatocytes with CDFDA dye (green). The exported fluorescent part (with cleaved diacetate part by the intercellular esterase activity) of the stain is visualized with the green signal. In the 3D cultures formation of canalicular network is evident (A) while in the monolayer cultures cells show insignificant bile canaliculi formation (B). The cell nuclei have been stained with hoechst (blue). Arrows show the exerted bile to the canaliculi network. (Scale = 50 μm)

Chapter 7

Conclusions and future work

The work I have done in my thesis focuses on experimental validation of microfluidic devices to test chemical and drug compounds on single-cells and tissue-like microcultures. I constructed custom-made microfluidic devices with the ultimate goal of creating *in vitro* physiologically relevant systems to study the cytotoxicity effects of test drug compounds.

Single-cell extracellular perturbation studies were carried out in two different experimental approaches for time- and concentration dependent extracellular sodium arsenite exposure effects. In approach one, discussed in **paper I** we explained how the combination of optical tweezers and a 4-inlet microfluidic device was used to regulate the uptake of arsenite in single yeast cell. We showed that a 40-min-treatment of 0.1 mM and 0.5 mM arsenite under constant flow rate of 1 μl min^{-1} induced Hsp104-GFP aggregation formation in the cells with concentration-dependent tendency. We observed a distinct heterogeneity in cellular responses to the treatment. We further showed that without any genetic intervention and by applying a controlled co-administration of a Hog1 inhibitor with a pre-incubation step of 5 min and concentration of 10 μM, the percentage of cells showing aggregates was elevated from 50 % to 80 %. Our data showed that the maximum number of aggregates per cell increased by 50 %.

In **papers II and III** I broadened the approach used in **paper I** to a microfluidic device that overcame the limitations of the previous experimental setting in cell and fluid handling. In **paper I** the throughput of the studies was limited to one field of view of the camera, a limited number of 25 cells in each run and impractical to carry out with mammalian cells. The cell loading with optical tweezers was tedious and rather complex. Specifically for a non-native user, operation of the system was technically challenging. The possibility of photo-damaging the cells by the focused laser light added another limitation to cell handling. I designed and fabricated a microfluidic device, CellComb, with 104 individual microtraps. A single device could be sequentially imaged in 13 sections along the x axis, with each section incorporating 8 microtraps in the field of view of the camera. Cells could be loaded in a simple step and the device increased the throughput of the experiments significantly to up to 625 cells with full capacity of a single device. Using the

CellComb device, I could induce flow-rate dependent Hsp104-GFP protein foci in the trapped yeast cells. The results showed that cells were more susceptible to arsenite toxicity in the low flow rate condition (25 nl min^{-1}) and demonstrated a larger degree of protein damage compared to the high flow rate condition (100 nl min^{-1}).

In this device I incorporated 2-μm-wide passages adjacent with two side channels. The flow of drug and nutrient molecules could be transported in and out of the central channel and facilitated an additional degree of flexibility to control the microfluidic environment. By injecting the compounds through the inlet of the central channel cells could be exposed to the test compounds by convective flow while local exposure of the trapped cells was feasible through the neighboring channels. By increasing the flow rates in the side channels by 2-3 folds compared to the central channel (e.g. 300 nl min^{-1} in the side channels - 150 nl min^{-1} in the central channel), local exposure of the cells to fluorescein solution as a drug surrogate for visualization purposes, was demonstrated in **paper II**. Additionally, NIH/3T3 were seeded into the microfluidic devices. This was the first step in transforming the experimental systems for conducting more complex experimental plans with mammalian cells in our lab. This design principle served as inspiration and the motivation to promote the diffusion-based mass transport cell culture chambers that were developed further in **paper IV** to an organ-on-a-chip microfluidic device.

In **paper IV** the possibilities of the microfluidic devices developed previously were expanded to an integrated platform with the ultimate goal of building the compartments for an integrated human-based *in vitro* multi-organ system. I chose to develop the device to mimic the geometrical as well as convection-diffusion mass transport of a classic liver lobule. The cell culture chambers were arranged in a honeycomb layout. Each honeycomb chamber had a diameter of 1.2-2.4 mm, mimicking the geometrical constraints of a classic liver lobule. The diffusion-dominated cell media circulation in the device conveyed nutrients to the culture chambers via 2-μm-wide passages. The microscope imaging of the morphological changes alongside cell staining with fluorescent dyes revealed the promotion of 3D tissue-like structure formation in the device. HepG2 and hiPSC-derived hepatocytes were cultured in the devices for periods of up to three weeks. Formation of bile canaliculi network was observed in the hiPSC-derived hepatocytes on various days of culture (e.g. day 8 and day 16) while it was absent in the 2D monolayer cultures.

The intertwined nature of environmental arsenic pollution with human health and the possibilities of therapeutic applications of the compound opens up an interesting and critical research field to understand and control the mechanisms of arsenite toxicity in cells. I believe that using microfluidic dynamic cellular environment in combination with single-cell analysis to study arsenite cytotoxicity in mammalian cells is imperative. The reproduction of the results with the homologue proteins in mammalian and human cells will reveal interesting results. Up-scaling the CellComb device in an integrated layout to enable screening of large numbers of cells must be considered. With the diffusion-based mass transport system sub-

stantially developed in the VLSLL device, single-cell studies on cell-cell interactions and intercellular synchronization can be conducted with modified designs of the CellComb device. Examples of such studies include the glycolytic oscillations and synchronization in single yeast and beta-cells. These experiments are currently under development in our research group.

The focus of the future work with VLSLL device must be on validating the platform with high throughput testing of drugs. Investigating the capabilities of the device in identifying cytotoxicity of established and unknown hepatotoxic drugs as well as comparisons between the cultures of PHH and hiPSC-hepatocytes should be performed.

Currently, I am evaluating the responses of long-term cultures of hiPSC-derived hepatocytes to substrate and inducer drugs of CYP 3A4 and CYP 2C9 enzymes. Dose-response studies with known hepatotoxic drugs such as diclofenac is also under evaluation. Additionally, I am conducting experiments on co-culturing hiPSC-derived hepatocytes with NPCs of the liver. These studies are expected to develop the physiological aspect of the platform from a single cell type to an organotypic niche and promote the interactions of different liver cells to represent a robust *in vitro* model system.

Another interesting area of study will be the integration of VLSLL device with other OOC platforms such as kidney and gut to create a relevant model for the complete drug clearance circle. Studying DILI in presence of other organ compartments such as heart or blood-brain barrier and the interplay of these compartments will certainly be interesting. The combination of the VLSLL device with hiPSC-derived disease models will open up another interesting line of research. The future of personalized medicine relies heavily on the development of *in vitro* screening systems which not only are capable of conducting high throughput ADMET studies but are also capable of representing patient-specific physiologically relevant characteristics.

Multi-organ, human-on-a-chip and patient-on-a-chip microphysiological platforms will experience a vast development and revolutionize the process of drug discovery as we know it today.

Chapter 8

Acknowledgements

The journey of my doctoral studies has certainly been one of the most demanding and yet thrilling endeavors I have had in my life. During my time as a PhD student I have faced many challenging moments and a handful of euphoria moments. I am grateful for all of it, if not more for the difficult times, as they have pushed me to my boundaries and helped me grow. But the most important part of this experience has been the people I have encountered and been inspired by.

Firstly, I would like to express my deepest gratitude to Dr. Mattias Goksör, my supervisor and my mentor for the opportunity he provided for me to do my PhD studies. I am thankful for all your invaluable guidance, advice and the unprejudiced and empowering approach in your role as my PhD supervisor. And most importantly for your friendship and hospitality.

Special thanks to my co-supervisor, Dr. Caroline B. Adiels. You have been present and witnessed most parts of the everyday hustle in the lab. I am truly grateful for all I learned from you. I am specifically thankful to you for introducing me to the fascinating world of biology and the very first trials you encouraged me through my clumsy pipetting skills.

To all present and former members of the Biological Physics lab, it has been a delight getting to know you and working alongside you. Martin Mojica Benavides and Philip Dalsbecker it's been fun to share the office with you and discuss research.

Dr. Martin Persson, Dr. Anna Karin Gustavsson, Ricardo Silva and Dr. Jonas Danielson it was a great pleasure to work with you in a fun and exciting environment. New members of the lab, Dr. Giovanni Volpe, Aykut Argun, Falko Schmidt, Saga Helgadóttir, thank you for the fun coffee breaks amid the tiring period of writing the thesis.

I would like to extend my gratitude to my examiner Prof. Johan Åkerman. I would like to acknowledge Dr. Maria Smedh at the CCI center for the help and the training with the confocal microscopy.

I would like to acknowledge all the staff in the MC2 nanofabrication lab at Chalmers for the help in the cleanroom.

I would like to thank all the great people, former and present, in the administration at the department of physics. Johanna Gustavsson, Maria Siirak, Bea Tensfeldt,

Mattias Zackrisson, Karin Lindqvist and Clara Wilow Sundh, I appreciate all the help I received from you every single time I knocked on your door.

My dearest friends, without whom I wouldn't be who I am today. To my two best friends Amir and Hadi, your friendship and the great memories we created in the undergraduate time have always been with me.

Kaveh and Babak, thank you for your deep-rooted and fun friendship. Also for our amazing time in Barcelona and the Andalusia adventure. Hessam and Dorreh, for never forgetting about me although I rarely could join you in the past year, well, because I was busy running experiments in the lab.

Saleh, you have been a true friend, when you were here in Gothenburg and also when you moved to the end of the world in NewZealand and made yourself unreachable. Our plans to visit the Kangaroos is still hanging.

Jannick, thank you for all the science we have done together and for the valuable comments on the thesis. More importantly for the amazing Caipirinhas you made and heavenly macadamia nuts...you're welcome to randomly send me more of them! and don't forget...you better finish strong ;)

Bruno, special thanks to you for all our superhero movie sessions. And thank you for hosting all our game nights, It has been fun with you, Renaud and Alex. We should kickstart it again.

Dr. Doryaneh Ahmadpour and Dr. Roja Babazadeh thank you for our pizza lunches and inspiring scientific discussions.

Dr. Sviatlana Shashkova, thank you for always being a true friend and for our fun Fikas and passionate tangos.

Many thanks to Jurgita Paukštytė, you taught me a great deal in biology and enzyme handling. And of course the pizza and beer nights at Foxes. Wish you success in your coming PhD studies.

The last but not least, I would like to extend my deepest gratitude to my family. To my father, Mohammad, who has been the very backbone of my education, for always providing me with opportunities to grow out of my comfort zone. And most importantly for your sacrifice for the past very very long years of living apart. I would also like to mention my dear departed mother, Habibeh, for all the love, support, inspiration and encouragement she provided for me. You are present in my life every single day. My dearest and only sister in the world, Nazanin, I'm happy to be the big brother :) and I'm happy to have you in my life, as you are my closest friend and the greatest sister. Wish you all the best in your own adventure. My deep and special thanks to my dearest uncle, Mohammad, and my best aunts, Farideh, Hosnieh, Sorayya and Saeideh, without your support and care I would not have made it this far.

Göteborg, February 24, 2017
Amin A. Banaeiyan

References

[1] M. W. Taylor, A history of cell culture, In *Viruses and Man: A History of Interactions*, pages 41–52, Springer (2014).

[2] R. Edmondson, J. J. Broglie, A. F. Adcock, and L. Yang, Three-dimensional cell culture systems and their applications in drug discovery and cell-based biosensors, *Assay and drug development technologies* **12**, 207–218 (2014).

[3] N. Kaplowitz, Idiosyncratic drug hepatotoxicity, *Nature Reviews Drug Discovery* **4**, 489–499 (2005).

[4] V. Sharma and J. H. McNeill, To scale or not to scale: the principles of dose extrapolation, *British journal of pharmacology* **157**, 907–921 (2009).

[5] U. Alon, *An introduction to systems biology: design principles of biological circuits*, CRC press (2006).

[6] H. Kitano, Systems biology: a brief overview, *Science* **295**, 1662–1664 (2002).

[7] H. Kitano, Computational systems biology, *Nature* **420**, 206–210 (2002).

[8] E. C. Butcher, E. L. Berg, and E. J. Kunkel, Systems biology in drug discovery, *Nature biotechnology* **22**, 1253–1259 (2004).

[9] P. S. Swain, M. B. Elowitz, and E. D. Siggia, Intrinsic and extrinsic contributions to stochasticity in gene expression, *Proceedings of the National Academy of Sciences* **99**, 12795–12800 (2002).

[10] I. G. Johnston, B. Gaal, R. P. das Neves, T. Enver, F. J. Iborra, and N. S. Jones, Mitochondrial variability as a source of extrinsic cellular noise, *PLoS Comput Biol* **8**, e1002416 (2012).

[11] M. B. Elowitz, A. J. Levine, E. D. Siggia, and P. S. Swain, Stochastic gene expression in a single cell, *Science* **297**, 1183–1186 (2002).

[12] A. Raj and A. van Oudenaarden, Nature, nurture, or chance: stochastic gene expression and its consequences, *Cell* **135**, 216–226 (2008).

[13] D. Longo and J. Hasty, Dynamics of single-cell gene expression, *Molecular Systems Biology* **2**, 64 (2006).

[14] P. L. Bedard, A. R. Hansen, M. J. Ratain, and L. L. Siu, Tumour heterogeneity in the clinic, *Nature* **501**, 355–364 (2013).

[15] A. Saadatpour, S. Lai, G. Guo, and G.-C. Yuan, Single-cell analysis in cancer genomics, *Trends in Genetics* **31**, 576–586 (2015).

[16] L. A. Herzenberg, D. Parks, B. Sahaf, O. Perez, M. Roederer, and L. A. Herzenberg, The history and future of the fluorescence activated cell sorter and flow cytometry: a view from Stanford, *Clinical chemistry* **48**, 1819–1827 (2002).

[17] B. P. Cormack, R. H. Valdivia, and S. Falkow, FACS-optimized mutants of the green fluorescent protein (GFP), *Gene* **173**, 33–38 (1996).

[18] R. Amann and B. M. Fuchs, Single-cell identification in microbial communities by improved fluorescence in situ hybridization techniques, *Nature Reviews Microbiology* **6**, 339–348 (2008).

[19] J. Lee, Y. H. Foong, I. Musaitif, T. Tong, and C. Jefcoate, Analysis of specific RNA in cultured cells through quantitative integration of q-PCR and N-SIM single cell FISH images: Application to hormonal stimulation of StAR transcription, *Molecular and cellular endocrinology* **429**, 93–105 (2016).

[20] B. Sakmann and E. Neher, Patch clamp techniques for studying ionic channels in excitable membranes, *Annual review of physiology* **46**, 455–472 (1984).

[21] J. Eberwine, H. Yeh, K. Miyashiro, Y. Cao, S. Nair, R. Finnell, M. Zettel, and P. Coleman, Analysis of gene expression in single live neurons, *Proceedings of the National Academy of Sciences* **89**, 3010–3014 (1992).

[22] J. Fuzik, A. Zeisel, Z. Máté, D. Calvigioni, Y. Yanagawa, G. Szabó, S. Linnarsson, and T. Harkany, Integration of electrophysiological recordings with single-cell RNA-seq data identifies neuronal subtypes, *Nature biotechnology* **34**, 175–183 (2016).

[23] T. M. Squires and S. R. Quake, Microfluidics: Fluid physics at the nanoliter scale, *Reviews of modern physics* **77**, 977 (2005).

[24] G. M. Whitesides, The origins and the future of microfluidics, *Nature* **442**, 368–373 (2006).

[25] P. S. Dittrich and A. Manz, Lab-on-a-chip: microfluidics in drug discovery, *Nature Reviews Drug Discovery* **5**, 210–218 (2006).

[26] P. C. Li, *Microfluidic lab-on-a-chip for chemical and biological analysis and discovery*, CRC press (2005).

[27] D. Figeys and D. Pinto, Lab-on-a-chip: a revolution in biological and medical sciences., *Analytical Chemistry* **72**, 330–A (2000).

[28] A. J. Demello, Control and detection of chemical reactions in microfluidic systems., *Nature* **442**, 394–402 (2006).

[29] D. D. Carlo and L. P. Lee, Dynamic single-cell analysis for quantitative biology, *Analytical chemistry* **78**, 7918–7925 (2006).

[30] J. R. Heath, A. Ribas, and P. S. Mischel, Single-cell analysis tools for drug discovery and development, *Nature Reviews Drug Discovery* **15**, 204–216 (2016).

[31] H. Yin and D. Marshall, Microfluidics for single cell analysis, *Current opinion in biotechnology* **23**, 110–119 (2012).

[32] V. Lecault, A. K. White, A. Singhal, and C. L. Hansen, Microfluidic single cell analysis: from promise to practice, *Current opinion in chemical biology* **16**, 381–390 (2012).

[33] X. Ding, S.-C. S. Lin, B. Kiraly, H. Yue, S. Li, I.-K. Chiang, J. Shi, S. J. Benkovic, and T. J. Huang, On-chip manipulation of single microparticles, cells, and organisms using surface acoustic waves, *Proceedings of the National Academy of Sciences* **109**, 11105–11109 (2012).

[34] N. Pamme and C. Wilhelm, Continuous sorting of magnetic cells via on-chip free-flow magnetophoresis, *Lab on a Chip* **6**, 974–980 (2006).

[35] X. Hu, P. H. Bessette, J. Qian, C. D. Meinhart, P. S. Daugherty, and H. T. Soh, Marker-specific sorting of rare cells using dielectrophoresis, *Proceedings of the National Academy of Sciences of the United States of America* **102**, 15757–15761 (2005).

[36] J. W. Hong, V. Studer, G. Hang, W. F. Anderson, and S. R. Quake, A nanoliter-scale nucleic acid processor with parallel architecture, *Nature biotechnology* **22**, 435–439 (2004).

[37] M. A. Unger, H.-P. Chou, T. Thorsen, A. Scherer, and S. R. Quake, Monolithic microfabricated valves and pumps by multilayer soft lithography, *Science* **288**, 113–116 (2000).

[38] R. A. Kellogg, R. Gómez-Sjöberg, A. A. Leyrat, and S. Tay, High-throughput microfluidic single-cell analysis pipeline for studies of signaling dynamics, *Nature protocols* **9**, 1713–1726 (2014).

[39] C. Zhang, D. Xing, and Y. Li, Micropumps, microvalves, and micromixers within PCR microfluidic chips: advances and trends, *Biotechnology advances* **25**, 483–514 (2007).

[40] C. Zhang, J. Xu, W. Ma, and W. Zheng, PCR microfluidic devices for DNA amplification, *Biotechnology advances* **24**, 243–284 (2006).

[41] F. A. Gomez, *Biological applications of microfluidics*, John Wiley & Sons (2008).

[42] S. N. Bhatia and D. E. Ingber, Microfluidic organs-on-chips, *Nature biotechnology* **32**, 760–772 (2014).

[43] E. L. LeCluyse, R. P. Witek, M. E. Andersen, and M. J. Powers, Organotypic liver culture models: meeting current challenges in toxicity testing, *Critical reviews in toxicology* **42**, 501–548 (2012).

[44] L. Richert, M. J. Liguori, C. Abadie, B. Heyd, G. Mantion, N. Halkic, and J. F. Waring, Gene expression in human hepatocytes in suspension after isolation is similar to the liver of origin, is not affected by hepatocyte cold storage and cryopreservation, but is strongly changed after hepatocyte plating, *Drug metabolism and disposition* **34**, 870–879 (2006).

[45] A. Dash, M. B. Simmers, T. G. Deering, D. J. Berry, R. E. Feaver, N. E. Hastings, T. L. Pruett, E. L. LeCluyse, B. R. Blackman, and B. R. Wamhoff, Hemodynamic flow improves rat hepatocyte morphology, function, and metabolic activity in vitro, *American Journal of Physiology-Cell Physiology* **304**, C1053–C1063 (2013).

[46] K. Funatsu, H. Ijima, K. Nakazawa, Y.-i. Yamashita, M. Shimada, and K. Sugimachi, Hybrid artificial liver using hepatocyte organoid culture, *Artificial organs* **25**, 194–200 (2001).

[47] S. Agastin, U.-B. T. Giang, Y. Geng, L. A. DeLouise, and M. R. King, Continuously perfused microbubble array for 3D tumor spheroid model, *Biomicrofluidics* **5**, 024110 (2011).

[48] B. Chevallay and D. Herbage, Collagen-based biomaterials as 3D scaffold for cell cultures: applications for tissue engineering and gene therapy, *Medical and Biological Engineering and Computing* **38**, 211–218 (2000).

[49] S. R. Khetani and S. N. Bhatia, Microscale culture of human liver cells for drug development, *Nature biotechnology* **26**, 120–126 (2008).

[50] D. Huh, B. D. Matthews, A. Mammoto, M. Montoya-Zavala, H. Y. Hsin, and D. E. Ingber, Reconstituting organ-level lung functions on a chip, *Science* **328**, 1662–1668 (2010).

[51] K.-J. Jang, A. P. Mehr, G. A. Hamilton, L. A. McPartlin, S. Chung, K.-Y. Suh, and D. E. Ingber, Human kidney proximal tubule-on-a-chip for drug transport and nephrotoxicity assessment, *Integrative Biology* **5**, 1119–1129 (2013).

[52] H. J. Kim, D. Huh, G. Hamilton, and D. E. Ingber, Human gut-on-a-chip inhabited by microbial flora that experiences intestinal peristalsis-like motions and flow, *Lab on a chip* **12**, 2165–2174 (2012).

[53] S.-A. Lee, E. Kang, J. Ju, D.-S. Kim, S.-H. Lee, *et al.*, Spheroid-based three-dimensional liver-on-a-chip to investigate hepatocyte–hepatic stellate cell interactions and flow effects, *Lab on a Chip* **13**, 3529–3537 (2013).

[54] I. Maschmeyer, A. K. Lorenz, K. Schimek, T. Hasenberg, A. P. Ramme, J. Hübner, M. Lindner, C. Drewell, S. Bauer, A. Thomas, *et al.*, A four-organ-chip for interconnected long-term co-culture of human intestine, liver, skin and kidney equivalents, *Lab on a Chip* **15**, 2688–2699 (2015).

[55] E. Novik, T. J. Maguire, P. Chao, K. Cheng, and M. L. Yarmush, A microfluidic hepatic coculture platform for cell-based drug metabolism studies, *Biochemical pharmacology* **79**, 1036–1044 (2010).

[56] J. Castillo-León and W. E. Svendsen, *Lab-on-a-Chip Devices and Micro-Total Analysis Systems: A Practical Guide*, Springer (2014).

[57] G. M. Whitesides and A. D. Stroock, Flexible methods for microfluidics, *Phys. Today* **54**, 42–48 (2001).

[58] A. D. Stroock and G. M. Whitesides, Components for integrated poly (dimethylsiloxane) microfluidic systems, *Electrophoresis* **23**, 3461–3473 (2002).

[59] A. Author, Single cells or large populations?, *Lab on a Chip* **7**, 544–546 (2007).

[60] S.-Y. Teh, R. Lin, L.-H. Hung, and A. P. Lee, Droplet microfluidics, *Lab on a Chip* **8**, 198–220 (2008).

[61] I. Barbulovic-Nad, S. H. Au, and A. R. Wheeler, A microfluidic platform for complete mammalian cell culture, *Lab on a Chip* **10**, 1536–1542 (2010).

[62] N. R. Pollock, J. P. Rolland, S. Kumar, P. D. Beattie, S. Jain, F. Noubary, V. L. Wong, R. A. Pohlmann, U. S. Ryan, and G. M. Whitesides, A paper-based multiplexed transaminase test for low-cost, point-of-care liver function testing, *Science translational medicine* **4**, 152ra129–152ra129 (2012).

[63] C. Liu, M. Mauk, R. Gross, F. D. Bushman, P. H. Edelstein, R. G. Collman, and H. H. Bau, Membrane-based, sedimentation-assisted plasma separator for point-of-care applications, *Analytical chemistry* **85**, 10463–10470 (2013).

[64] J. Hu, S. Wang, L. Wang, F. Li, B. Pingguan-Murphy, T. J. Lu, and F. Xu, Advances in paper-based point-of-care diagnostics, *Biosensors and Bioelectronics* **54**, 585–597 (2014).

[65] M. M. Thuo, R. V. Martinez, W.-J. Lan, X. Liu, J. Barber, M. B. Atkinson, D. Bandarage, J.-F. Bloch, and G. M. Whitesides, Fabrication of low-cost paper-based microfluidic devices by embossing or cut-and-stack methods, *Chemistry of Materials* **26**, 4230–4237 (2014).

[66] R. Novak, N. Ranu, and R. A. Mathies, Rapid fabrication of nickel molds for prototyping embossed plastic microfluidic devices, *Lab on a chip* **13**, 1468–1471 (2013).

[67] C. M. B. Ho, S. H. Ng, K. H. H. Li, and Y.-J. Yoon, 3D printed microfluidics for biological applications, *Lab on a Chip* **15**, 3627–3637 (2015).

[68] D. Huh, G. A. Hamilton, and D. E. Ingber, From 3D cell culture to organs-on-chips, *Trends in cell biology* **21**, 745–754 (2011).

[69] P. J. Lee, P. J. Hung, and L. P. Lee, An artificial liver sinusoid with a microfluidic endothelial-like barrier for primary hepatocyte culture, *Biotechnology and bioengineering* **97**, 1340–1346 (2007).

[70] K. Domansky, W. Inman, J. Serdy, A. Dash, M. H. Lim, and L. G. Griffith, Perfused multiwell plate for 3D liver tissue engineering, *Lab on a chip* **10**, 51–58 (2010).

[71] D. Elger, B. Williams, C. Crowe, and R. J.A., *Engineering Fluid Mechanics, 10th Edition*, Wiley Global Education (2012).

[72] E. K. Sackmann, A. L. Fulton, and D. J. Beebe, The present and future role of microfluidics in biomedical research, *Nature* **507**, 181–189 (2014).

[73] G. K. Batchelor, *An introduction to fluid dynamics*, Cambridge university press (2000).

[74] J. H. Ferziger and M. Peric, *Computational methods for fluid dynamics*, Springer Science & Business Media (2012).

[75] D. J. Tritton, *Physical fluid dynamics*, Springer Science & Business Media (2012).

[76] N.-T. Nguyen and S. T. Wereley, *Fundamentals and applications of microfluidics*, Artech House (2002).

[77] D. G. Grier, A revolution in optical manipulation, *Nature* **424**, 810–816 (2003).

[78] A. Jonáš and P. Zemanek, Light at work: The use of optical forces for particle manipulation, sorting, and analysis, *Electrophoresis* **29**, 4813–4851 (2008).

[79] A. Ashkin and J. Dziedzic, Optical trapping and manipulation of viruses and bacteria, *Science* **235**, 1517–1520 (1987).

[80] A. Ashkin, J. Dziedzic, and T. Yamane, Optical trapping and manipulation of single cells using infrared laser beams, *Nature* **330**, 769–771 (1987).

[81] A.-K. Gustavsson, D. D. van Niekerk, C. B. Adiels, F. B. du Preez, M. Goksör, and J. L. Snoep, Sustained glycolytic oscillations in individual isolated yeast cells, *Febs Journal* **279**, 2837–2847 (2012).

[82] C. H. Blomqvist, P. Dinér, M. Grøtli, M. Goksör, and C. B. Adiels, A single-cell study of a highly effective Hog1 inhibitor for in situ yeast cell manipulation, *Micromachines* **5**, 81–96 (2014).

[83] X. Wang, X. Gou, S. Chen, X. Yan, and D. Sun, Cell manipulation tool with combined microwell array and optical tweezers for cell isolation and deposition, *Journal of Micromechanics and Microengineering* **23**, 075006 (2013).

[84] J. Sleep, D. Wilson, R. Simmons, and W. Gratzer, Elasticity of the red cell membrane and its relation to hemolytic disorders: an optical tweezers study, *Biophysical journal* **77**, 3085–3095 (1999).

[85] M. Dao, C. T. Lim, and S. Suresh, Mechanics of the human red blood cell deformed by optical tweezers, *Journal of the Mechanics and Physics of Solids* **51**, 2259–2280 (2003).

[86] R. Agrawal, T. Smart, J. Nobre-Cardoso, C. Richards, R. Bhatnagar, A. Tufail, D. Shima, P. H. Jones, and C. Pavesio, Assessment of red blood cell deformability in type 2 diabetes mellitus and diabetic retinopathy by dual optical tweezers stretching technique, *Scientific reports* **6** (2016).

[87] B. Pontes, N. Viana, L. Salgado, M. Farina, V. M. Neto, and H. Nussenzveig, Cell cytoskeleton and tether extraction, *Biophysical journal* **101**, 43–52 (2011).

[88] S. Chen, J. Cheng, C.-W. Kong, X. Wang, S. H. Cheng, R. A. Li, and D. Sun, Laser-induced fusion of human embryonic stem cells with optical tweezers, *Applied Physics Letters* **103**, 033701 (2013).

[89] M.-C. Zhong, X.-B. Wei, J.-H. Zhou, Z.-Q. Wang, and Y.-M. Li, Trapping red blood cells in living animals using optical tweezers, *Nature communications* **4**, 1768 (2013).

[90] E. D'Este, G. Baj, P. Beuzer, E. Ferrari, G. Pinato, E. Tongiorgi, and D. Cojoc, Use of optical tweezers technology for long-term, focal stimulation of specific subcellular neuronal compartments, *Integrative Biology* **3**, 568–577 (2011).

[91] Y. Wang, E. L. Botvinick, Y. Zhao, M. W. Berns, S. Usami, R. Y. Tsien, and S. Chien, Visualizing the mechanical activation of Src, *Nature* **434**, 1040–1045 (2005).

[92] B. Shergill, L. Meloty-Kapella, A. A. Musse, G. Weinmaster, and E. Botvinick, Optical tweezers studies on Notch: single-molecule interaction strength is independent of ligand endocytosis, *Developmental cell* **22**, 1313–1320 (2012).

[93] A. Ashkin, J. Dziedzic, J. Bjorkholm, and S. Chu, Observation of a single-beam gradient force optical trap for dielectric particles, *Optics letters* **11**, 288–290 (1986).

[94] A. Ashkin, *Optical trapping and manipulation of neutral particles using lasers: a reprint volume with commentaries*, World Scientific (2006).

[95] G. Gouesbet, B. Maheu, and G. Gréhan, Light scattering from a sphere arbitrarily located in a Gaussian beam, using a Bromwich formulation, *JOSA A* **5**, 1427–1443 (1988).

[96] T. Tlusty, A. Meller, and R. Bar-Ziv, Optical gradient forces of strongly localized fields, *Physical review letters* **81**, 1738 (1998).

[97] J. W. Lichtman and J.-A. Conchello, Fluorescence microscopy, *Nature methods* **2**, 910–919 (2005).

[98] D. B. Murphy, *Fundamentals of light microscopy and electronic imaging*, John Wiley & Sons (2002).

[99] J. T. Watson and O. D. Sparkman, *Introduction to mass spectrometry: instrumentation, applications, and strategies for data interpretation*, John Wiley & Sons (2007).

[100] M. Rodahl, F. Höök, A. Krozer, P. Brzezinski, and B. Kasemo, Quartz crystal microbalance setup for frequency and Q-factor measurements in gaseous and liquid environments, *Review of Scientific Instruments* **66**, 3924–3930 (1995).

[101] J. Homola, S. S. Yee, and G. Gauglitz, Surface plasmon resonance sensors: review, *Sensors and Actuators B: Chemical* **54**, 3–15 (1999).

[102] A. Periasamy, *Methods in cellular imaging*, Springer (2013).

[103] R. Niedenthal, L. Riles, M. Johnston, and J. Hegemann, Green fluorescent protein as a marker for gene expression and subcellular localization in budding yeast, *Yeast* **12**, 773–786 (1996).

[104] A. Jaboski, Efficiency of anti-Stokes fluorescence in dyes, *Nature* **131**, 21 (1933).

[105] J. B. Pawley, editor, *Handbook Of Biological Confocal Microscopy*, Springer Science & Business Media (2006).

[106] R. K. Mortimer, Evolution and variation of the yeast (Saccharomyces) genome, *Genome Research* **10**, 403–409 (2000).

[107] A. Goffeau, B. G. Barrell, H. Bussey, R. Davis, *et al.*, Life with 6000 genes, *Science* **274**, 546 (1996).

[108] D. Botstein and G. R. Fink, Yeast: an experimental organism for 21st Century biology, *Genetics* **189**, 695–704 (2011).

[109] D. Petranovic and J. Nielsen, Can yeast systems biology contribute to the understanding of human disease?, *Trends in biotechnology* **26**, 584–590 (2008).

[110] A. H. Kachroo, J. M. Laurent, C. M. Yellman, A. G. Meyer, C. O. Wilke, and E. M. Marcotte, Systematic humanization of yeast genes reveals conserved functions and genetic modularity, *Science* **348**, 921–925 (2015).

[111] P. Bharadwaj, R. Martins, and I. Macreadie, Yeast as a model for studying Alzheimer's disease, *FEMS yeast research* **10**, 961–969 (2010).

[112] S. Treusch, S. Hamamichi, J. L. Goodman, K. E. Matlack, C. Y. Chung, V. Baru, J. M. Shulman, A. Parrado, B. J. Bevis, J. S. Valastyan, *et al.*, Functional links between Aβ toxicity, endocytic trafficking, and Alzheimer′s disease risk factors in yeast, *Science* **334**, 1241–1245 (2011).

[113] C. Vacher, L. Garcia-Oroz, and D. C. Rubinsztein, Overexpression of yeast hsp104 reduces polyglutamine aggregation and prolongs survival of a transgenic mouse model of Huntington's disease, *Human molecular genetics* **14**, 3425–3433 (2005).

[114] S. Krobitsch and S. Lindquist, Aggregation of huntingtin in yeast varies with the length of the polyglutamine expansion and the expression of chaperone proteins, *Proceedings of the National Academy of Sciences* **97**, 1589–1594 (2000).

[115] P. M. Joyner, R. M. Matheke, L. M. Smith, and R. H. Cichewicz, Probing the metabolic aberrations underlying mutant huntingtin toxicity in yeast and assessing their degree of preservation in humans and mice, *Journal of proteome research* **9**, 404–412 (2009).

[116] D. Carmona-Gutierrez, T. Eisenberg, S. Büttner, C. Meisinger, G. Kroemer, and F. Madeo, Apoptosis in yeast: triggers, pathways, subroutines, *Cell Death & Differentiation* **17**, 763–773 (2010).

[117] V. D. Longo, G. S. Shadel, M. Kaeberlein, and B. Kennedy, Replicative and chronological aging in Saccharomyces cerevisiae, *Cell metabolism* **16**, 18–31 (2012).

[118] G. E. Janssens, A. C. Meinema, J. González, J. C. Wolters, A. Schmidt, V. Guryev, R. Bischoff, E. C. Wit, L. M. Veenhoff, and M. Heinemann, Protein biogenesis machinery is a driver of replicative aging in yeast, *eLife* **4**, e08527 (2015).

[119] H. Dihazi, R. Kessler, and K. Eschrich, High osmolarity glycerol (HOG) pathway-induced phosphorylation and activation of 6-phosphofructo-2-kinase are essential for glycerol accumulation and yeast cell proliferation under hyperosmotic stress, *Journal of Biological Chemistry* **279**, 23961–23968 (2004).

[120] V. Reiser, H. Ruis, and G. Ammerer, Kinase activity-dependent nuclear export opposes stress-induced nuclear accumulation and retention of Hog1 mitogen-activated protein kinase in the budding yeast Saccharomyces cerevisiae, *Molecular Biology of the Cell* **10**, 1147–1161 (1999).

[121] J. Albertyn, S. Hohmann, J. M. Thevelein, and B. A. Prior, GPD1, which encodes glycerol-3-phosphate dehydrogenase, is essential for growth under osmotic stress in Saccharomyces cerevisiae, and its expression is regulated by the high-osmolarity glycerol response pathway., *Molecular and cellular biology* **14**, 4135–4144 (1994).

[122] P. Dinér, J. V. Vilg, J. Kjellén, I. Migdal, T. Andersson, M. Gebbia, G. Giaever, C. Nislow, S. Hohmann, R. Wysocki, *et al.*, Design, synthesis, and characterization of a highly effective Hog1 inhibitor: a powerful tool for analyzing MAP kinase signaling in yeast, *PloS one* **6**, e20012 (2011).

[123] J. L. Boyer, Bile formation and secretion, *Comprehensive physiology* **3**, 1035–1078 (2013).

[124] P. Godoy, N. J. Hewitt, U. Albrecht, M. E. Andersen, N. Ansari, S. Bhattacharya, J. G. Bode, J. Bolleyn, C. Borner, J. Böttger, *et al.*, Recent advances in 2D and 3D in vitro systems using primary hepatocytes, alternative hepatocyte sources and non-parenchymal liver cells and their use in investigating mechanisms of hepatotoxicity, cell signaling and ADME, *Archives of toxicology* **87**, 1315–1530 (2013).

[125] B. Bacon and J. O'Grady, *Comprehensive Clinical Hepatology*, number v. 1 in Comprehensive Clinical Hepatology, Elsevier Mosby (2006).

[126] E. Kuntz and H.-D. Kuntz, *Hepatology: Textbook and atlas*, Springer Science & Business Media (2009).

[127] E. Wisse, R. De Zanger, K. Charels, P. Van Der Smissen, and R. McCuskey, The liver sieve: considerations concerning the structure and function of endothelial fenestrae, the sinusoidal wall and the space of Disse, *Hepatology* **5**, 683–692 (1985).

[128] R. Li, A. Oteiza, K. K. Sørensen, P. McCourt, R. Olsen, B. Smedsrød, and D. Svistounov, Role of liver sinusoidal endothelial cells and stabilins in elimination of oxidized low-density lipoproteins, *American Journal of Physiology-Gastrointestinal and Liver Physiology* **300**, G71–G81 (2011).

[129] R. A. Roberts, P. E. Ganey, C. Ju, L. M. Kamendulis, I. Rusyn, and J. E. Klaunig, Role of the Kupffer cell in mediating hepatic toxicity and carcinogenesis, *Toxicological Sciences* **96**, 2–15 (2007).

[130] R. Bataller and D. A. Brenner, Liver fibrosis, *The Journal of clinical investigation* **115**, 209–218 (2005).

[131] P. O'brien, W. Irwin, D. Diaz, E. Howard-Cofield, C. Krejsa, M. Slaughter, B. Gao, N. Kaludercic, A. Angeline, P. Bernardi, *et al.*, High concordance of drug-induced human hepatotoxicity with in vitro cytotoxicity measured in a novel cell-based model using high content screening, *Archives of toxicology* **80**, 580–604 (2006).

[132] C. C. Bell, D. F. Hendriks, S. M. Moro, E. Ellis, J. Walsh, A. Renblom, L. F. Puigvert, A. C. Dankers, F. Jacobs, J. Snoeys, *et al.*, Characterization of primary human hepatocyte spheroids as a model system for drug-induced liver injury, liver function and disease, *Scientific reports* **6** (2016).

[133] N. J. Hewitt, M. J. Gómez Lechón, J. B. Houston, D. Hallifax, H. S. Brown, P. Maurel, J. G. Kenna, L. Gustavsson, C. Lohmann, C. Skonberg, *et al.*, Primary hepatocytes: current understanding of the regulation of metabolic enzymes and transporter proteins, and pharmaceutical practice for the use of hepatocytes in metabolism, enzyme induction, transporter, clearance, and hepatotoxicity studies, *Drug metabolism reviews* **39**, 159–234 (2007).

[134] A. A. Palakkan, D. C. Hay, K. TV, and J. A. Ross, Liver tissue engineering and cell sources: issues and challenges, *Liver International* **33**, 666–676 (2013).

[135] S. Wilkening, F. Stahl, and A. Bader, Comparison of primary human hepatocytes and hepatoma cell line Hepg2 with regard to their biotransformation properties, *Drug Metabolism and Disposition* **31**, 1035–1042 (2003).

[136] H. Gerets, K. Tilmant, B. Gerin, H. Chanteux, B. Depelchin, S. Dhalluin, and F. Atienzar, Characterization of primary human hepatocytes, HepG2 cells, and HepaRG cells at the mRNA level and CYP activity in response to inducers and their predictivity for the detection of human hepatotoxins, *Cell biology and toxicology* **28**, 69–87 (2012).

[137] A. Guillouzo, A. Corlu, C. Aninat, D. Glaise, F. Morel, and C. Guguen-Guillouzo, The human hepatoma HepaRG cells: a highly differentiated model for studies of liver metabolism and toxicity of xenobiotics, *Chemico-biological interactions* **168**, 66–73 (2007).

[138] K. Takahashi and S. Yamanaka, Induction of pluripotent stem cells from mouse embryonic and adult fibroblast cultures by defined factors, *cell* **126**, 663–676 (2006).

[139] R. Schwartz, H. Fleming, S. Khetani, and S. Bhatia, Pluripotent stem cell-derived hepatocyte-like cells, *Biotechnology advances* **32**, 504–513 (2014).

[140] Y. Tanaka, M. Yamato, T. Okano, T. Kitamori, and K. Sato, Evaluation of effects of shear stress on hepatocytes by a microchip-based system, *Measurement Science and Technology* **17**, 3167 (2006).

[141] C. Hayden, J. Eijkel, and C. Dalton, An alternative method of fabricating sub-micron resolution masks using excimer laser ablation, *Journal of Micromechanics and Microengineering* **14**, 826 (2004).

[142] S. Mitra and S. K. Chakraborty, SU-8 photolithography and its impact on microfluidics, In *Microfluidics and Nanofluidics Handbook: Fabrication, Implementation, and Applications*, volume 2, pages 231–268, CRC Press: Boca Raton, FL, USA (2011).

[143] M. A. Eddings, M. A. Johnson, and B. K. Gale, Determining the optimal PDMS–PDMS bonding technique for microfluidic devices, *Journal of Micromechanics and Microengineering* **18**, 067001 (2008).

[144] E. Eriksson, J. Enger, B. Nordlander, N. Erjavec, K. Ramser, M. Goksör, S. Hohmann, T. Nyström, and D. Hanstorp, A microfluidic system in combination with optical tweezers for analyzing rapid and reversible cytological alterations in single cells upon environmental changes, *Lab on a Chip* **7**, 71–76 (2007).

[145] E. Eriksson, K. Sott, F. Lundqvist, M. Sveningsson, J. Scrimgeour, D. Hanstorp, M. Goksör, and A. Granéli, A microfluidic device for reversible environmental changes around single cells using optical tweezers for cell selection and positioning, *Lab on a Chip* **10**, 617–625 (2010).

[146] P. Dinér, J. V. Vilg, J. Kjellén, I. Migdal, T. Andersson, M. Gebbia, G. Giaever, C. Nislow, S. Hohmann, R. Wysocki, *et al.*, Design, synthesis, and characterization of a highly effective Hog1 inhibitor: a powerful tool for analyzing MAP kinase signaling in yeast, *PloS one* **6**, e20012 (2011).

[147] M. Smedh, C. Beck, K. Sott, and M. Goksör, CellStress-open source image analysis program for single-cell analysis, In *SPIE NanoScience + Engineering*, pages 77622N–77622N, International Society for Optics and Photonics (2010).

[148] M. Kvarnström, K. Logg, A. Diez, K. Bodvard, and M. Käll, Image analysis algorithms for cell contour recognition in budding yeast, *Optics Express* **16**, 12943–12957 (2008).

[149] D. R. Berger, B. R. Ware, M. D. Davidson, S. R. Allsup, and S. R. Khetani, Enhancing the functional maturity of induced pluripotent stem cell–derived human hepatocytes by controlled presentation of cell–cell interactions in vitro, *Hepatology* **61**, 1370–1381 (2015).